

Muon $g-2$ and a type-X two-Higgs-doublet scenario: Some studies in high-scale validity

Atri Dey,^{1,*} Jayita Lahiri,^{2,†} and Biswarup Mukhopadhyaya^{3,‡}

¹Regional Centre for Accelerator-based Particle Physics, Harish-Chandra Research Institute, HBNI, Chhatnag Road, Jhansi, Allahabad 211 019, India

²Department of Physics, Indian Institute of Technology Guwahati, North Guwahati, Assam 781039, India

³Department of Physical Sciences, Indian Institute of Science Education and Research Kolkata, Mohanpur 741246, India



(Received 21 January 2022; accepted 8 September 2022; published 20 September 2022)

We study the high-scale validity of a type-X two Higgs doublet scenario, which provides an explanation of the observed value of muon ($g-2$). This region allows a pseudoscalar physical state, which is well below the observed 125-GeV scalar in mass. A second neutral scalar particle can be both above and below 125 GeV in such a scenario. Admissible regions in the parameter space are obtained by using the most recent data on muon ($g-2$), theoretical constraints such as low-scale perturbativity and vacuum stability, and also all experimental constraints, including the available LHC results. Among other things, both the aforesaid orders of CP -even neutral scalar masses are included in our benchmark studies. Two-loop renormalization group equations are used to predict the values of various couplings at high scales, and the regions in the space spanned by low-scale parameters, which retain perturbative unitarity as well as vacuum stability up to various scales are identified. We thus conclude that such a scenario, while successfully explaining the observed muon ($g-2$), can be valid up to energy scales ranging from 10^4 GeV to the Planck scale, thus opening up directions of thought on its ultraviolet completion.

DOI: [10.1103/PhysRevD.106.055023](https://doi.org/10.1103/PhysRevD.106.055023)

I. INTRODUCTION

It is often speculated that the spontaneous symmetry-breaking sector of the electroweak theory may include additional ingredients, over and above the single complex Higgs doublet postulated in the “minimal” original framework. The simplest and most obvious extension is a scenario with two complex scalar doublets. The spectrum of physical fields in such a case, after the absorption of three Goldstone bosons, consists of two CP -even neutral scalars, one CP -odd neutral scalar and a pair of mutually conjugate charged scalar bosons. While the doublets can both acquire vacuum expectation values in such a scenario, the Yukawa couplings to fermions are more model specific, depending on the various possibilities restricted by the principle of natural flavour conservation. Various phenomenological features of

a two Higgs doublet model (2HDM) are accordingly decided.

A scenario of particular interest is the type-X 2HDM where one of the scalar doublets couples only to quarks, and the other, to leptons. The doublet that couples to quarks dominates the mass eigenstate corresponding to the 125-GeV scalar that has been experimentally discovered. We are concerned with this kind of a theory in the present work.

A rather striking consequence of a type-X 2HDM is that it admits of scalar physical states considerably lighter than 125 GeV, consistently with all experimental observations so far. In particular, the neutral pseudoscalar here can be well below 100 GeV. This is worthy of special mention because such a light pseudoscalar can mediate contributions to the muon anomalous magnetic moment, leading to a closer agreement with the experimental observation [1–3]. Keeping this in mind, the region of the parameter space answering to such a light pseudoscalar has been investigated from various angles in recent times, including its implications for the LHC [4–19].

Let us now motivate the present study, which is centered around an examination of the type-X 2HDM spectrum and interactions at higher energy scales. We start by remembering the various other scenarios beyond the standard model, which have been invoked to explain the observed value of

*atridey@hri.res.in

†jayitalahiri@iitg@rd.ac.in

‡biswarup@iiserkol.ac.in

Published by the American Physical Society under the terms of the [Creative Commons Attribution 4.0 International license](https://creativecommons.org/licenses/by/4.0/). Further distribution of this work must maintain attribution to the author(s) and the published article's title, journal citation, and DOI. Funded by SCOAP³.

muon ($g - 2$). As randomly chosen samples, these include, among many others

- (i) Supersymmetry (SUSY) [20].
- (ii) Left-right symmetric models [21].
- (iii) Scenarios with exotic (vectorlike) fermions [22].
- (iv) Scenarios with dark photons [23].
- (v) Seesaw models [24,25].

If we look at them in turn, all of the above scenarios admit ultraviolet (UV) completion in some way or the other. SUSY can be embedded in a grand unified theory (GUT) or in high-scale scenarios like those based on supergravity. Left-right symmetric theories can emerge as low-energy limits of popular GUT theories such as $SO(10)$. Vectorlike fermions occur in the fundamental representation of E_6 GUT. Dark photons, too, arise out of an additional $U(1)$, which in turn can be the artifact of GUT models with symmetry breaking at intermediate scales.

While the minimal SUSY standard model subsumes a type-II 2HDM, no such obvious connection with a UV complete scenario is noticeable for a type-X 2HDM. It is therefore an important question to ask whether the type-X scenario, while providing an explanation of muon ($g - 2$), is also capable of merger with any popular high-scale scenario, for, in that case the subtle discrepancy in a low-energy phenomenon would be traceable to ultraviolet physics. In order for that to happen, however, the corresponding type-X 2HDM parameter space needs to be consistent, among other things, with theoretical constraints such as vacuum stability or perturbative unitarity, all the way to the scale of the aforesaid new physics. If, on the other hand, such constraints indicate a relatively low cutoff for type-X 2HDM, then one senses the presence of additional physics at an intermediate scale, before its merger into any popular high-scale scheme (such as GUT) is conceivable.

The above question can be settled by (1) precisely identifying regions in the parameter space of a type-X 2HDM answering to the latest measurement of muon ($g - 2$), (2) running the low-scale parameters of the scalar potential to progressively high energy scales, and (3) checking whether the issues of vacuum stability or perturbative unitarity lead to upper limits of validity for various benchmark regions in the parameter space. This is the hitherto unaccomplished task that has been performed in the current work.

The type-X 2HDM scenario is, according to several extant studies, amenable to election in TeV-scale collider experiments. This is possible through not only a light pseudoscalar state but also via searches for the corresponding charged scalar. The details of the observable phenomenology depend on the values of the various parameters that enter into the arena. To study them, one naturally seeks consistency with the latest muon ($g - 2$) data. With this in view, even before addressing the main question mentioned

above, we have first updated the allowed region in light of that data. While many studies have explicitly shown only the dominant Feynman diagrams contributing to the anomalous magnetic moment of muon, we have thoroughly considered the contributions from all possible diagrams. In addition, we have included both the possibilities of the 125-GeV state being the lighter (possible decoupling of the extended scalar sector) or the heavier (nondecoupling of the extended scalar sector) one between the two neutral CP -even physical fields. In addition, the Yukawa interactions of spin-zero states being of either the same sign or of the opposite sign with respect to the couplings to gauge boson pairs are considered.

We would like to mention here that studies in the past have explored type-X 2HDM in the context of muon ($g - 2$). We have made identification of right- and wrong-sign Yukawa couplings as well as the possibilities of the 125 GeV scalar being the lighter/heavier CP -even state, in the context of type-X 2HDM. We have performed an exhaustive analysis in this work, taking into account all such possibilities and presented the allowed region of parameter space in each of these scenarios, in a bid to finally unfold the UV completion of each scenarios.

Having thus set the stage, the question we ask here is this: Can the aforesaid aspects of low-energy phenomenology provide any hint of the UV completion of this scenario? If so, then not only does the muon anomalous magnetic moment get related to high-scale physics, but we also build towards some insights into features such as the signs of Yukawa interactions at low energy or the possible decoupling or nondecoupling structure of the extended scalar sector. With this in view, we have undertaken a detailed study of the high-scale behavior of the various quartic couplings in the scalar potential of the type-X 2HDM. Limits on its high-scale validity then arise from vacuum stability, perturbativity, and unitarity of the couplings. This exercise has been carried out across various regions of the parameter space, including both right- and wrong-sign Yukawa interaction regions, where the muon anomalous magnetic moment is better explained, and all other theoretical and experimental constraints are satisfied. We make use of two-loop renormalization group (RG) equations. However, it is demonstrated in some illustrative cases that the difference in the results is not qualitative, as compared to those obtained with one-loop RG equations (RGEs). Therefore, the explanation of the allowed regions of the parameter space corresponding to various levels of high-scale validity has been often given by referring to the one-loop RGs where the effects of different parameters of the theory are more transparent.

The plan of this work is as follows. In Sec. II, we discuss the type-X two Higgs doublet model and its various aspects relevant for our analysis. Section III summarizes the implications of the observed muon ($g - 2$) for this specific model. We discuss various theoretical and experimental

constraints on this model and the allowed parameter space in Sec. IV. In Sec. V, we study the renormalization group evolution of various couplings for a few benchmarks. We next identify in Sec. VI, the regions of parameter space which are valid up to various high scales and are also interesting from the perspective of the anomalous magnetic moment of muon as well as relevant collider searches. This way we try to explore the validity of type-X 2HDM as a UV-complete theory. Finally, we conclude our analysis in Sec. VII.

II. TYPE-X TWO HIGGS DOUBLET MODEL

The most general scalar potential involving two scalar doublets with hypercharge $Y = 1$, under the assumption of a softly broken discrete Z_2 symmetry, is given by [26]

$$\begin{aligned} \mathcal{V} = & m_{11}^2(\Phi_1^\dagger\Phi_1) + m_{22}^2(\Phi_2^\dagger\Phi_2) - [m_{12}^2(\Phi_1^\dagger\Phi_2 + \text{H.c.})] \\ & + \frac{\lambda_1}{2}(\Phi_1^\dagger\Phi_1)^2 + \frac{\lambda_2}{2}(\Phi_2^\dagger\Phi_2)^2 + \lambda_3(\Phi_1^\dagger\Phi_1)(\Phi_2^\dagger\Phi_2) \\ & + \lambda_4(\Phi_1^\dagger\Phi_2)(\Phi_2^\dagger\Phi_1) + \left[\frac{\lambda_5}{2}(\Phi_1^\dagger\Phi_2)^2 + \text{H.c.} \right]. \end{aligned} \quad (1)$$

We assume CP conservation, in which case all λ_i s and m_{12}^2 are real.

The two complex Higgs doublets with hypercharge $Y = 1$ can be written as

$$\begin{aligned} \Phi_1 &= \begin{pmatrix} \phi_1^+ \\ \frac{1}{\sqrt{2}}(v_1 + \phi_1^0 + ia_1) \end{pmatrix}, \\ \Phi_2 &= \begin{pmatrix} \phi_2^+ \\ \frac{1}{\sqrt{2}}(v_2 + \phi_2^0 + ia_2) \end{pmatrix}. \end{aligned} \quad (2)$$

Where v_1 and v_2 are the vacuum expectation values with $v^2 = v_1^2 + v_2^2 = (246 \text{ GeV})^2$ and $\tan\beta = v_2/v_1$. After electroweak symmetry breaking, we obtain five physical states, two neutral CP -even scalars, the lighter of which will be called h , and the heavier H , one neutral pseudoscalar A , and a pair of charged scalars H^\pm .

In type-X 2HDM the Yukawa interactions can be given as

$$\begin{aligned} -\mathcal{L}_{\text{Yukawa}} = & Y_{u2}\bar{Q}_L\tilde{\Phi}_2u_R + Y_{d2}\bar{Q}_L\Phi_2d_R \\ & + Y_{\ell1}\bar{L}_L\Phi_1e_R + \text{H.c.} \end{aligned} \quad (3)$$

in which $Q_L^T = (u_L, d_L)$, $L_L^T = (\nu_L, l_L)$, and $\tilde{\Phi}_{1,2} = i\tau_2\Phi_{1,2}^*$. Y_{u2} , Y_{d2} , and $Y_{\ell1}$ are the couplings of the up, down quarks and leptons with the two doublets, family indices are suppressed.

The factors by which the standard model (SM) Higgs interaction strengths need to be scaled to obtain the neutral scalar Yukawa couplings are

$$\begin{aligned} y_h^{fi} &= [\sin(\beta - \alpha) + \cos(\beta - \alpha)\kappa_f], \\ y_H^{fi} &= [\cos(\beta - \alpha) - \sin(\beta - \alpha)\kappa_f], \\ y_A^{fi} &= -i\kappa_f \text{ (for } u), \quad y_A^{fi} = i\kappa_f \text{ (for } d, \ell), \end{aligned}$$

$$\text{with } \kappa_\ell \equiv -\tan\beta, \quad \kappa_u = \kappa_d \equiv 1/\tan\beta. \quad (4)$$

The corresponding charged Higgs Yukawa couplings are

$$\begin{aligned} \mathcal{L}_Y = & -\frac{\sqrt{2}}{v}H^+\{\bar{u}_i[\kappa_d(V_{\text{CKM}})_{ij}m_{d_j}P_R \\ & - \kappa_u m_{ui}(V_{\text{CKM}})_{ij}P_L]d_j + \kappa_\ell\bar{\nu}_m\ell P_R\ell\} + \text{H.c.}, \end{aligned} \quad (5)$$

in which $i, j = 1, 2, 3$.

The couplings of gauge boson pairs with the neutral scalars are given by

$$y_h^V = \sin(\beta - \alpha) \times g_{\text{SM}}^V, \quad y_H^V = \cos(\beta - \alpha) \times g_{\text{SM}}^V, \quad (6)$$

Where V denotes W or Z and g_{SM}^V is the coupling strength of the SM Higgs with a gauge boson pair.

Furthermore, Yukawa couplings here may or may not have the same sign as in the SM case [27],

$$\begin{aligned} y_h^{fi} \times y_h^V &> 0 \text{ for SM-like coupling or right-sign (RS),} \\ y_h^{fi} \times y_h^V &< 0 \text{ for wrong-sign (WS).} \end{aligned} \quad (7)$$

This can happen, for example, for down-type Yukawa couplings in type II 2HDM [27] as well. However, in type-X 2HDM the wrong-sign Yukawa coupling can arise in the lepton Yukawa sector alone, unless one allows $\tan\beta < 1$. In the case of SM-like coupling, the 125-GeV Higgs couplings are very close to those in the SM, which is the so-called alignment limit. Now in the wrong-sign regime, the absolute values of y_h^ℓ and y_h^V should still be close to unity because of the restrictions of 125-GeV Higgs signal data [28,29]. Moreover, there are two scenarios: (1) The lightest CP -even scalar h is SM-like, i.e., $m_h = m_{h_{\text{SM}}} = 125 \text{ GeV}$, we call this scenario 1 and (2) when the heavier CP -even scalar H is SM-like, i.e., $m_H = m_{h_{\text{SM}}} = 125 \text{ GeV}$, we call this scenario 2. Both scenarios 1 and 2 can in principle lead to right sign or wrong sign of Yukawa coupling depending on the conditions stated in Eq. (7).

Let us first consider scenario 1 in the right- and wrong-sign regions. In scenario 1, the 125-GeV Higgs couplings are

$$y_h^\ell = \sin(\beta - \alpha) - \cos(\beta - \alpha)\tan\beta, \quad y_h^V \simeq \sin(\beta - \alpha).$$

In the alignment limit $|\sin(\beta - \alpha)| \approx 1$. The following possibilities emerge depending on the sign of $\sin(\beta - \alpha)$ and range of $\tan\beta$.

- (1) For $\sin(\beta - \alpha) < 0$, $\cos(\beta - \alpha) > 0$, y_h^ℓ takes the form $-(1 + \epsilon)$. $y_h^\ell \times y_h^V > 0$ and it corresponds to right-sign region.
- (2) On the other hand, for $\sin(\beta - \alpha) > 0$, $\cos(\beta - \alpha) > 0$, y_h^ℓ takes the form $(1 - \epsilon)$. This case also corresponds to the right-sign region.
- (3) When $\sin(\beta - \alpha) > 0$ and $\cos(\beta - \alpha) > 0$ and $\tan\beta \gtrsim 10$, y_h^ℓ becomes negative and $y_h^\ell \times y_h^V < 0$. This scenario gives rise to wrong-sign lepton-Yukawa coupling.

Having discussed the coupling structure in scenario 1, we will now explore the same for scenario 2. In this case, the heavier CP -even Higgs is the observed 125 GeV Higgs, i.e., $m_H = 125$ GeV. Here the couplings of H with the leptons and gauge bosons take the following forms.

$$y_H^\ell = \cos(\beta - \alpha) + \sin(\beta - \alpha)\tan\beta, \quad y_h^V \simeq \cos(\beta - \alpha)$$

In the alignment limit, $|\sin(\beta - \alpha)| \ll 1$. The sign of $\sin(\beta - \alpha)$ and ranges of $\tan\beta$ in this case will give rise to the following conditions:

- (1) For $\sin(\beta - \alpha) > 0$, $\cos(\beta - \alpha) > 0$, y_H^ℓ takes the form $(1 + \epsilon)$ and $y_H^\ell \times y_H^V > 0$. Therefore this case corresponds to the right-sign region.
- (2) On the other hand, for $\sin(\beta - \alpha) < 0$, $\cos(\beta - \alpha) > 0$, y_H^ℓ takes the form $(1 - \epsilon)$, $y_H^\ell \times y_H^V > 0$. Hence this region also gives rise to right-sign lepton-Yukawa coupling.
- (3) When $\sin(\beta - \alpha) < 0$ and $\cos(\beta - \alpha) > 0$ and $\tan\beta \gtrsim 10$, y_H^ℓ becomes negative and $y_H^\ell \times y_H^V < 0$. In this scenario, wrong-sign condition is satisfied.

For the classification of wrong and right sign of Yukawa couplings in various parts of the parameter space, we present the aforementioned conditions in Table I.

Throughout the discussion concerning scenarios 1 and 2, ϵ is assumed to be an extremely small positive quantity. One should note that $\tan\beta (\gtrsim 10)$ in the right-sign region will give rise to Yukawa scale factors widely differing from unity (therefore disfavored by the Higgs signal strength data), unless $|\sin(\beta - \alpha)|$ (scenario 1) or $|\cos(\beta - \alpha)|$ (scenario 2) is very close to 1. Notably, $\cos(\beta - \alpha)$ is kept positive in all the above cases, since the signs of the Yukawa interactions are unambiguously decided by $(\beta - \alpha)$ lying in two of the four quadrants. The required ranges of $\tan\beta$ are not altered by such quadrant choice.

The main motivation of the present study is to explore the possibility of having a light ($\lesssim 100$ GeV) pseudoscalar in type-X 2HDM, which makes it easier to match the observed value of anomalous magnetic moment of muon (henceforth to be called $g_\mu - 2$). We will see in the following section that large $\tan\beta$ regions will be favored from this particular requirement. There will be further overlap or tension between various theoretical and experimental constraints on the model parameter space. These are decisive in understanding the high-scale validity of the scenario, which is our ultimate purpose here.

III. EXPLANATION OF $g_\mu - 2$

The anomalous magnetic moment of muon is an early triumph of quantum field theory. In today's context, the long-standing discrepancy between SM prediction and experimental observation [30] hints towards new physics. The recent result from Fermilab [2,3] has strengthened this disagreement further. The future E34 experiment at J-PARC [31] may shed new light on this tension between theory and experiment.

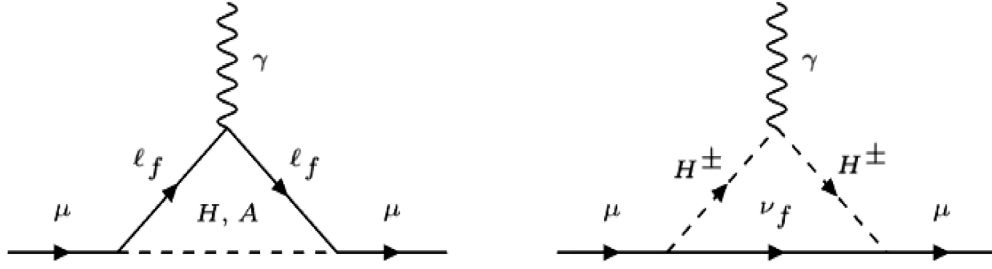
The effect of loop corrections are usually parameterized in terms of $a_\mu = \frac{g_\mu - 2}{2}$. The SM contributions to $a_\mu = \frac{g_\mu - 2}{2}$ have been extensively studied [32–54], the most recent estimate [55] being

$$a_\mu^{\text{SM}} = 116591810(43) \times 10^{-11}. \quad (8)$$

In [55], the combined contribution of QED, electroweak, and hadronic SM processes are discussed. The hadronic contribution is comprised of hadronic vacuum polarization (HVP) and hadronic light-by-light scattering. In determining HVP, data-driven methods are proven to be most effective [39,40]. Lattice QCD calculations are also available for HVP [56]. However, the currently available lattice results for HVP have a larger uncertainty compared to the data-driven ones according to [55]. On the other hand, hadronic light-by-light scattering has been calculated with both phenomenological approach [48,57] as well as lattice QCD [49,58]. Both methods are in agreement with each other and yield comparable precision. Hence a weighted average of the two results has been considered. We refer the reader to [55] (in particular their Sec. 8) for further discussion on the technicalities which are beyond the scope of the present paper.

TABLE I. The requirement for RS/WS regions as a function of the mass hierarchies as well as $\text{sgn}(\sin(\beta - \alpha))$ and $\text{sgn}(\cos(\beta - \alpha))$.

Mass hierarchy	$\text{sgn}(\sin(\beta - \alpha))$	$\text{sgn}(\cos(\beta - \alpha))$	Region
Scenario 1 ($m_h = 125$ GeV)	–	+	RS
Scenario 1 ($m_h = 125$ GeV)	+	+	RS/WS
Scenario 2 ($m_H = 125$ GeV)	+	+	RS
Scenario 2 ($m_H = 125$ GeV)	–	+	RS/WS


 FIG. 1. Nonstandard contribution to Δa_μ at one-loop.

While the most recent experimental bound [2] is obtained by combining the Fermilab data (2021) [3] and earlier BNL (2006) data [1]:

$$a_\mu^{\text{exp}} = 116592061(41) \times 10^{-11}. \quad (9)$$

This may be contrasted with the earlier limits from BNL data [1]:

$$a_\mu^{\text{exp-BNL}} = 116592089(63) \times 10^{-11}. \quad (10)$$

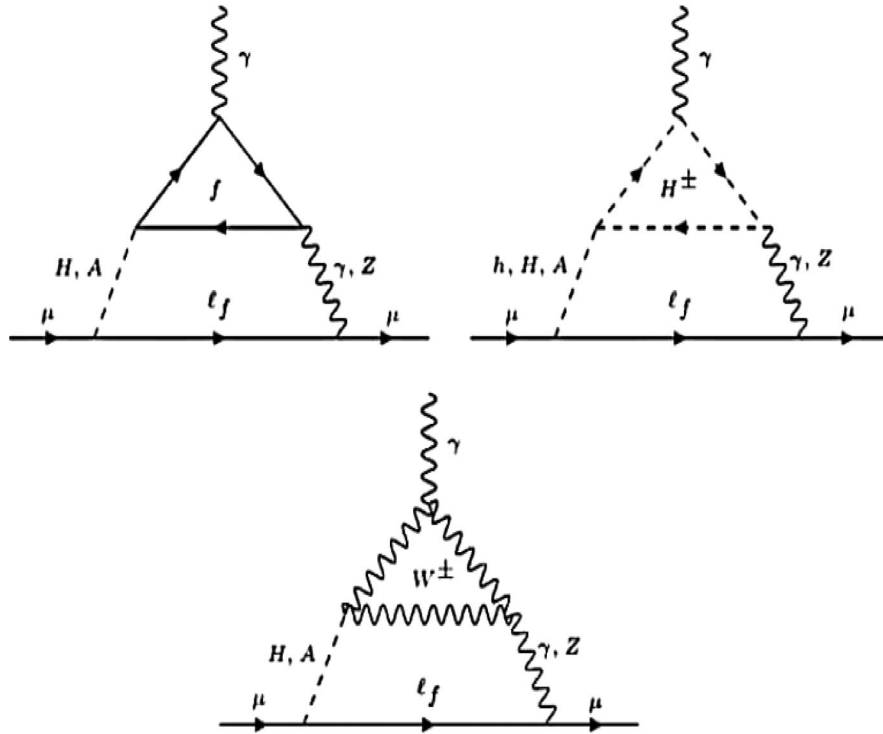
Thus there is approximately a 4.2σ discrepancy when one uses the combined experimental result [Eq. (9)]:

$$\Delta a_\mu = a_\mu^{\text{exp}} - a_\mu^{\text{SM}} = 251(59) \times 10^{-11}. \quad (11)$$

On the other hand, a discrepancy at the level of 3.7σ is seen, if one uses only the BNL data [Eq. (10)]:

$$\Delta a_\mu^{\text{BNL}} = a_\mu^{\text{exp-BNL}} - a_\mu^{\text{SM}} = 279(76) \times 10^{-11}. \quad (12)$$

We consider one loop as well as two loop Barr-Zee type contribution to Δa_μ in type-X 2HDM. It has been shown in earlier works [59,60], that the two-loop Barr-Zee diagrams dominate over the one-loop contributions, both of which are shown in Figs. 1–4. Although the two loop diagrams suffer from a loop suppression factor, they also have an enhancement factor of $\frac{M^2}{m_\mu^2}$, where M is the mass of the heavy particle running in the loop namely, t, b, τ, H^\pm, W^\pm (see Fig. 2). One should note that in type-X 2HDM, the contribution from the τ loop gets an additional enhancement factor from the τ coupling with pseudoscalar (A) in the large $\tan\beta$ region. The enhancement factor in general dominates over the aforementioned loop suppression. The diagram involving W^\pm in the loop (Fig. 2, bottom), will have negligible contribution due to suppression in the


 FIG. 2. Nonstandard contribution to Δa_μ from two-loop Barr-Zee diagrams with internal γ/Z .

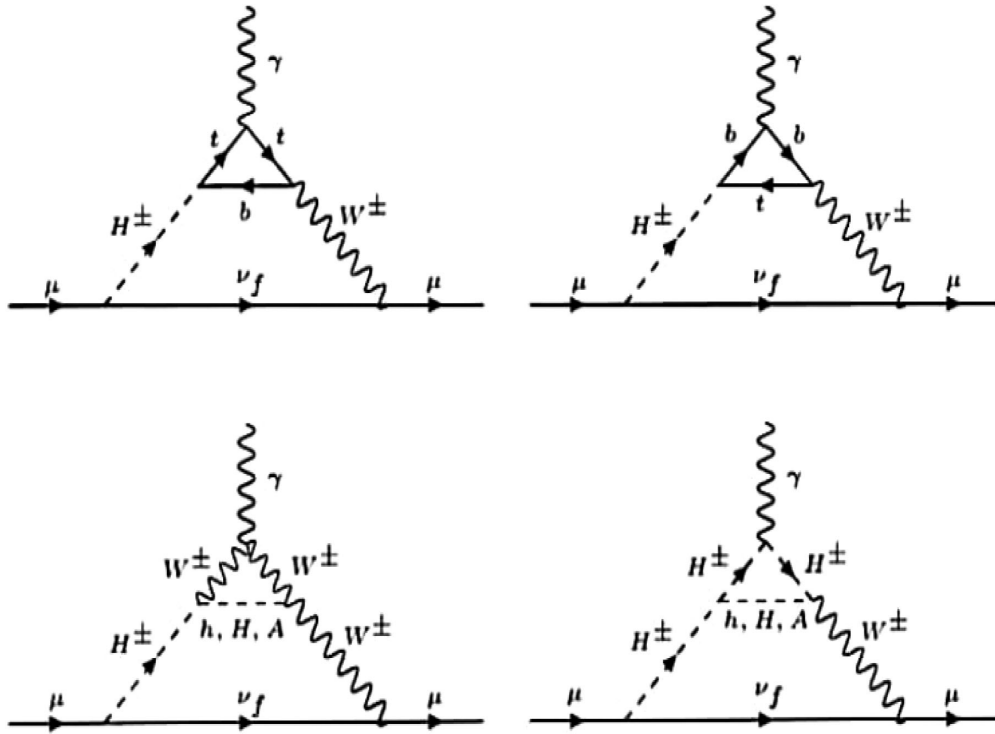


FIG. 3. Nonstandard contribution to Δa_μ from two-loop Barr-Zee diagrams with internal W^\pm and H^\pm . Cross-diagrams with H^\pm and W^\pm interchanged are also considered.

coupling between W^\pm bosons and the nonstandard CP -even Higgs in the alignment limit. We also consider the Barr-Zee diagrams where charged Higgs replaces the neutral Higgs and also W^\pm substitutes the internal γ (see Figs. 3 and 4). The contribution from these diagrams can be sizable in some regions of the parameter space [60].

In order to obtain updated constraints on Δa_μ , we have calculated afresh the contributions from all the aforementioned diagrams following [59,60]. The resulting constraints on the m_A - $\tan\beta$ plane is shown in Fig. 5. The 3σ upper and lower bound on the experimentally observed central value of Δa_μ have been used in the scan. We have (1) used the most recent $g_\mu - 2$ constraints and (2) taken into account the exhaustive set of one-loop diagrams and two-loop Barr-Zee diagrams in our analysis. In our scan, we have marginalized over all the model parameters except

m_A and $\tan\beta$ and also considered both right- and wrong-sign lepton-Yukawa couplings. Similar scans have been carried out earlier [61–63]. We would like to mention that one can in principle have additional contribution from two-loop non-Barr-Zee diagrams. But they will have negligible effect, as pointed out in [62].

In Fig. 5, the yellowish interior corresponds to the region that satisfies constraints coming from a combination of the BNL and Fermilab data. The red bands on both sides of this region, denote the additional regions which are allowed at the 3σ level before Fermilab data came into existence. The red band on the lower side is consistent even when the new data are included, so long as one allows experimental values to be undersaturated by type-X 2HDM. On the other hand, points in the upper red band overshoot the 3σ limit arising from the combined

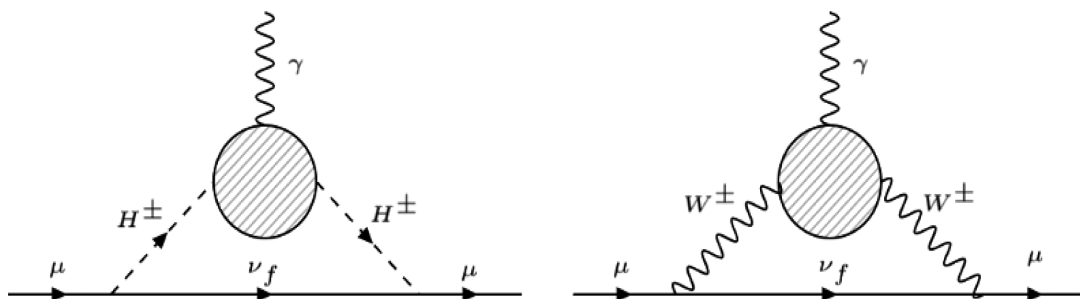


FIG. 4. Same as in Fig. 3, but with both internal lines $H^\pm H^\pm$ and $W^\pm W^\pm$.

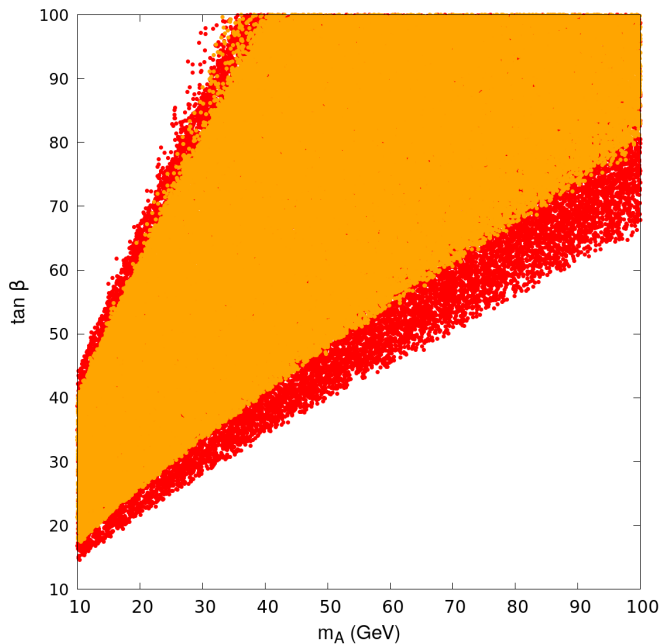


FIG. 5. The allowed region in $m_A - \tan\beta$ plane from $g_\mu - 2$ data at 3σ level. The limits have been obtained by marginalizing over all other parameters of the 2HDM, except the mass of one of the neutral CP -even scalars is set at 125 GeV. The nonstandard CP -even neutral scalar and charged scalar masses have been varied from 90 to 870 GeV. The yellowish interior corresponds to the combined constraints from older [1] and recent data [2,3], while the red regions on both sides show the additional regions allowed when only the older data are used.

data, and therefore, may be taken to be in conflict with the most recent experiments.

We mention here that, for the most part of our parameter space, the dominant two-loop contribution comes from the Barr-Zee diagrams involving τ loop. The other two-loop diagrams contribute $\lesssim 10\%$ of the Barr-Zee contribution. The one-loop diagrams, on the other hand, amount to $\sim 30\text{--}40\%$ of the two-loop Barr-Zee contribution but it comes with a relative negative sign with respect to the two-loop as well as total SM contribution.

It is clear that a low mass pseudoscalar with an enhanced coupling to the τ leptons, will give rise to a significant contribution to Δa_μ [see Fig. 2 (top left)], especially for large $\tan\beta$. Overall, low m_A and large $\tan\beta$ region is favored in the light of $g_\mu - 2$ data in our model. In this work, we are interested to know the high-scale behavior of this particular region of parameter space. Before exploring the high-scale validity of this region of the parameter space, we would like to consider the other important theoretical as well as experimental constraints on such a scenario.

IV. FIRST LEVEL OF FILTER: ALLOWED PARAMETER SPACE FROM LOW ENERGY DATA

In order to examine the possible UV completion of type-X 2HDM, especially in the region of parameter space

which nicely explains the observed $g_\mu - 2$, one needs to check the effects of various other constraints. For example, a pertinent question is this: Which parts of the model parameter space are valid from the perturbative unitarity and vacuum stability at the electroweak scale, so that the possibility of their UV completion can be tested. Another important question is this: Which parts of the parameter space that are valid up to high scales, are already ruled out by the experimental observations, and which parts can be probed in the near future. A thorough study of all the relevant theoretical and experimental constraints will be necessary to answer these questions. The analysis in this section is done with this motivation. We have divided our parameter space into categories, based on important features of the model, such as the sign of Yukawa coupling, decoupling/nondecoupling extended scalar sector, and studied the constraints on each of these categories, to have a better understanding of the interplay between various model parameters, while the constraints are imposed.

A. Constraints from electroweak precision observables

The custodial $SU(2)$ is a symmetry of the tree-level 2HDM potential and can be broken at the loop level due to corrections to weak boson masses as well as weak couplings by extra scalars in 2HDM (in addition to mass splitting between the two components in a fermion doublet). Electroweak precision measurements of the oblique parameters, have been performed by the Gfitter group [64]. This restricts the mass difference between the charged scalar and the nonstandard CP -even scalar $|\Delta m| = |m_{h/H} - m_{H^\pm}|$, depending on m_A and values of m_{H^\pm} [61]. The status of two Higgs doublet models in light of the global electroweak data has been presented in [65].

The allowed parameter space in $m_A - \Delta m$ plane is shown in Fig. 6 with color-coded representation of m_{H^\pm} . We mention here that, in order to take into account the

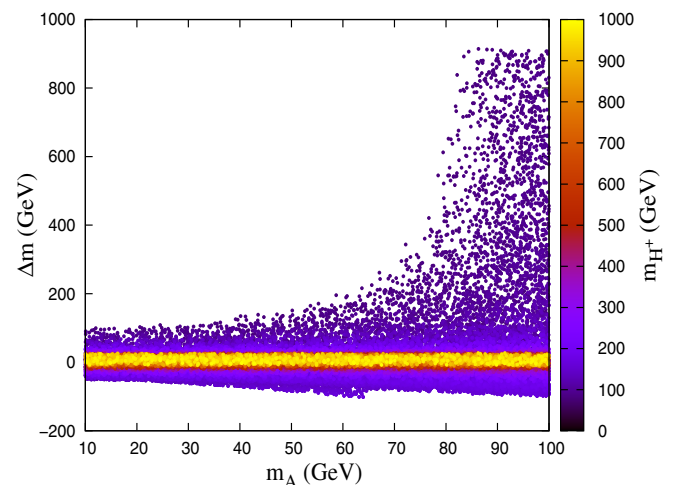


FIG. 6. The region allowed by S, T, U, V, W, X parameters on the $m_A - \Delta m$ plane, where m_{H^\pm} is shown as the color axis.

correlation between S and T parameters, we have considered the elliptic contour in the $S - T$ plane, computed with U as a free parameter within its experimentally allowed range. This choice leaves us with a less constrained parameter space than the scenario when U is fixed at 0. We have also taken into account the other Peskin-Takeuchi parameters (V , W , and X [66]) and the bounds coming from their measurement [67], since we are considering scalar masses below the EW scale. However, we found these parameters do not further constrain the parameter space, once the S , T parameter requirements are satisfied. This was also pointed out in [68]. The quantities S, T, U, V, W, X for our parameter space have been calculated using the package 2HDMC-1.8.0 [69].

We can see from Fig. 6, in the pseudoscalar mass range of our interest ($m_A \lesssim 100$ GeV), one can have $|\Delta m| \lesssim 50$ GeV with $m_H^\pm \lesssim 200$ GeV. The upper limit on $|\Delta m|$ becomes further stringent when $m_H^\pm \gtrsim 200$ GeV. However, large positive Δm (up to a TeV or so) is allowed when A and H^\pm are closely degenerate. This behavior can be understood from the mutual cancellation between terms in the calculation of T parameter, when either A or H is mass degenerate with H^\pm [70–72].

B. Constraints from lepton universality

In the SM τ decay takes place via W -boson exchange. In 2HDM, tree-level H^\pm exchange also contributes to leptonic τ decay. At one-loop level, the contribution to leptonic τ decay is dominated by τ -Yukawa coupling to $H^\pm/H/A$, which are essentially proportional to $(m_\tau^2/v^2)\tan^2\beta$. The one-loop diagrams contributing to the process are shown in [8]. It has been also pointed out there that other diagrams such as box diagrams give rise to subdominant contribution. The leptonic τ decay ($\tau \rightarrow \mu\nu_\mu\nu_\tau$) is parametrized in terms of a parameter $G_{\mu\tau}$, which is defined as

$$\left(\frac{G_{\mu\tau}}{G_F}\right)^2 = \frac{\Gamma(\tau \rightarrow \mu\nu_\tau\nu_\mu)_{2\text{HDM}}}{\Gamma(\tau \rightarrow \mu\nu_\tau\nu_\mu)_{\text{SM}}}. \quad (13)$$

On the other hand, since $m_e, m_\mu \ll m_\tau$, the analogous parameters $G_{e\mu}$, $G_{e\tau}$, corresponding to $\mu \rightarrow e\nu_e\nu_\mu$ and $\tau \rightarrow e\nu_e\nu_\tau$ decays are close to their SM values, i.e., $G_{e\mu} \approx G_{e\tau} \approx G_F$. The constraints on lepton universality from HFAG group [73] are as follows:

$$\frac{G_{\mu\tau}}{G_{e\mu}} = 1.0029 \pm 0.0015, \quad \frac{G_{\mu\tau}}{G_{e\tau}} = 1.0018 \pm 0.0014, \quad (14)$$

with their correlation coefficient 0.48. This constraints restrict the 2HDM parameter space, in particular, $g_\mu - 2$ allowed $m_A - \tan\beta$ plane depending on m_{H^\pm} and m_H . In the low m_{H^\pm} limit, the m_A and $\tan\beta$ get restricted to lower values. With higher values of m_{H^\pm} , larger m_A and $\tan\beta$ regions get allowed [8,19]. In our work, we have chosen

our benchmarks such that they are allowed by the aforementioned lepton universality constraints at the 3σ level.

We would like to mention that similar to τ decay, constraints also come from Z -decay width [especially $\Gamma(Z \rightarrow \tau\tau)$], which in 2HDM gets modified from their SM value, due to enhanced loop contribution coming from the extra scalars, especially in the large $\tan\beta$ region. However, it has been shown in [8] that, this constraint turns out to be much weaker compared to the τ -decay constraint and therefore is trivially satisfied for all our benchmarks.

C. Theoretical constraints

Theoretical constraints include perturbativity, unitarity, and vacuum stability conditions at the electroweak scale. Effects of these constraints on various 2HDMs have been studied in detail in earlier works [74–76]. It has been pointed out that a large separation between m_A and m_{H^\pm} is disfavored by the requirement of vacuum stability and perturbativity. We concentrate on the low m_A region and therefore it is crucial to look at the allowed upper limit on m_{H^\pm} in this scenario. We devote some discussion to these constraints because in the subsequent analysis we repeatedly check on the compliance with such constraints at various high energies, by running the parameters with the help of RG equations.

- (1) Perturbativity and unitarity: If 2HDM is a perturbative quantum field theory at a given scale, it would imply all quartic couplings $|C_{H_i H_j H_k H_l}| < 4\pi$ and all Yukawa couplings $|Y_j| < \sqrt{4\pi}$. Further, unitarity bound on the tree level scattering amplitude of the Higgses and longitudinal parts of EW gauge bosons put an upper bound on the eigenvalues $|a_i| \leq 8\pi$ of the $2 \rightarrow 2$ scattering matrices [77,78].

The physical masses can be written as a function of the quartic couplings in the following manner:

$$m_A^2 = \frac{m_{12}^2}{\sin\beta \cos\beta} - \lambda_5 v^2, \quad (15)$$

$$m_{H^\pm}^2 \approx m_A^2 + \frac{1}{2}v^2(\lambda_5 - \lambda_4). \quad (16)$$

It is clear from Eq. (16) that $m_{H^\pm}^2 - m_A^2$ is proportional to $\lambda_5 - \lambda_4$ which should be less than $\lambda_3 + \sqrt{\lambda_1 \lambda_2}$ from the requirement of vacuum stability [see Eq. (20)]. Therefore these conditions along with the requirement of perturbativity, i.e., $|C_{H_i H_j H_k H_l}| < 4\pi$ puts an upper limit on the mass square difference $m_{H^\pm}^2 - m_A^2$.

In what follows, we translate these constraints into those of the parameter space for both right- and wrong-sign Yukawa couplings. With this in view, we first express the quartic couplings in terms of physical masses and mixing angles.

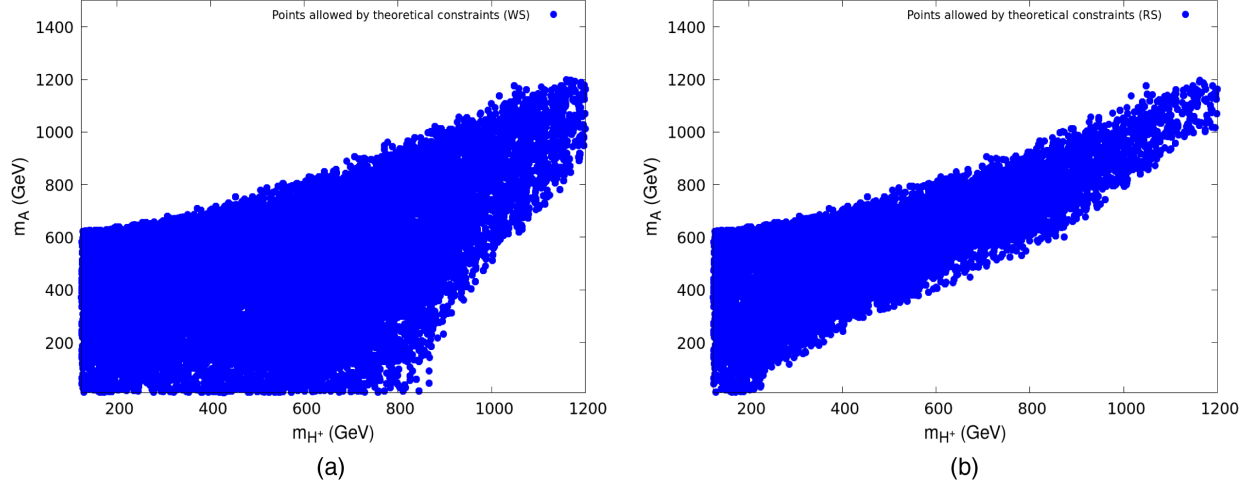


FIG. 7. Allowed parameter space in $m_{H^\pm} - m_A$ plane consistent with theoretical bounds in the (a) WS and (b) RS cases. The parameter space considered in the both of these figures correspond to scenarios 1 and 2 combined.

$$\lambda_1 = \frac{m_H^2 \cos^2 \alpha + m_h^2 \sin^2 \alpha - m_{12}^2 \tan \beta}{v^2 \cos^2 \beta}, \quad \lambda_{1,2} > 0, \quad (18)$$

$$\lambda_2 = \frac{m_H^2 \sin^2 \alpha + m_h^2 \cos^2 \alpha - m_{12}^2 \cot \beta}{v^2 \sin^2 \beta}, \quad \lambda_3 > -\sqrt{\lambda_1 \lambda_2}, \quad (19)$$

$$\lambda_3 = \frac{(m_H^2 - m_h^2) \cos \alpha \sin \alpha + 2m_{H^\pm}^2 \sin \beta \cos \beta - m_{12}^2}{v^2 \sin \beta \cos \beta}, \quad |\lambda_5| < \lambda_3 + \lambda_4 + \sqrt{\lambda_1 \lambda_2}. \quad (20)$$

$$\lambda_4 = \frac{(m_A^2 - 2m_{H^\pm}^2) \sin \beta \cos \beta + m_{12}^2}{v^2 \sin \beta \cos \beta},$$

$$\lambda_5 = \frac{m_{12}^2 - m_A^2 \sin \beta \cos \beta}{v^2 \sin \beta \cos \beta}. \quad (17)$$

It is clear from the expression of λ_1 in Eq. (17) that, to have it in the perturbative limit, the soft Z_2 breaking parameter $m_{12}^2 \approx \frac{m_h^2}{\tan \beta}$. Also the perturbativity condition of the quartic couplings λ_4 and λ_5 implies $m_{H^\pm}^2 - m_A^2 < 4\pi v^2$, which translates to the limit $m_{H^\pm} \lesssim 870$ GeV for very low m_A .

(2) Vacuum stability: Vacuum stability demands that there can exist no direction in the field space in which $\mathcal{V} \rightarrow -\infty$. This implies the following conditions on the quartic couplings of the Higgs potential [79–81].

The last condition in Eq. (20) can be rewritten as $\lambda_3 + \lambda_4 - \lambda_5 > -\sqrt{\lambda_1 \lambda_2}$ for $m_H > m_A$. One of the key features to note is that the upper limits on the heavy Higgs masses show quite different behaviors in the right-sign and wrong-sign limit of the Yukawa couplings [82]. The light-Higgs Yukawa couplings for leptons y_h^ℓ in type-X 2HDM can be expressed as

$$y_h^\ell = -\frac{\sin \alpha}{\cos \beta} \equiv \sin(\beta - \alpha) - \tan \beta \cos(\beta - \alpha). \quad (21)$$

The 125 GeV-Higgs boson couplings are experimentally found to be very much SM-like, implying, in particular, $|\sin(\beta - \alpha)| \simeq 1$ and $|y_h^\ell| \simeq 1$. This can be achieved when $\tan \beta \cos(\beta - \alpha) \approx 0$ (leading to the right-sign lepton coupling $y_h^\ell \approx +1$), or in the large $\tan \beta$ limit with $\tan \beta \cos(\beta - \alpha) \approx 2$ (leading to the wrong-sign coupling $y_h^\ell \approx -1$). Using the Eqs. (21) and (17), one finds [83]

$$\lambda_3 + \lambda_4 - \lambda_5 = \frac{2m_A^2 + y_h^\ell \sin(\beta - \alpha)m_h^2 - (\sin^2(\beta - \alpha) + y_h^\ell \sin(\beta - \alpha))m_H^2}{v^2} + \mathcal{O}\left(\frac{1}{\tan^2 \beta}\right) \quad (22)$$

in the large $\tan \beta$ limit. Now, in the right-sign case ($y_h^\ell \sin(\beta - \alpha) \rightarrow +1$), we have

$$2\frac{m_H^2}{v^2} < \sqrt{0.26 \times 4\pi} + \frac{2m_A^2 + m_h^2}{v^2}, \quad (23)$$

which puts a strong upper bound, $m_H \lesssim 250$ GeV for low m_A , which is consistent with [61]. On the other hand, in the wrong-sign limit ($y_h^\ell \sin(\beta - \alpha) \rightarrow -1$), m_H can be arbitrarily large with the condition $\sin^2(\beta - \alpha) + y_h^\ell \sin(\beta - \alpha) \approx 0$ being trivially satisfied in the alignment limit. These particular properties of wrong-sign and right-sign regions can be seen from Figs. 7(a) and 7(b).

D. Constraints from the direct search at colliders

1. LEP data

The earliest collider constraint on the masses of charged and neutral scalars came from the LEP experiments [84]. The charged Higgs has been searched for at LEP in the process $e^+e^- \rightarrow \gamma/Z \rightarrow H^+H^-$ with subsequent decay $H^\pm \rightarrow \tau^\pm\nu_\tau$. Direct search at LEP in this channel provides a lower limit on charged Higgs mass m_{H^\pm} as a function of $\text{BR}(H^\pm \rightarrow \tau^\pm\nu_\tau)$. The strongest bound results in $m_{H^\pm} \gtrsim 90$ GeV [84] at 95% C.L., considering $\text{BR}(H^\pm \rightarrow \tau\nu_\tau) \approx 100\%$. However, the upper limit varies only mildly with the $\text{BR}(H^\pm \rightarrow \tau\nu_\tau)$ and therefore is fairly model independent. On the other hand, another LEP search in the channel $pp \rightarrow hA \rightarrow 4\tau$ also puts an upper limit on $\text{BR}(h \rightarrow \tau^+\tau^-) \times \text{BR}(A \rightarrow \tau^+\tau^-) \times R_{hA}$ (mixing between two doublets) for $m_A + m_h$ up to 200 GeV [85].

2. LHC data on the SM-like Higgs

An important constraint comes from the direct search for 125-GeV Higgs decaying into two light pseudoscalar final states when it is kinematically allowed. The upper bound on this branching ratio puts a severe constraint on the parameter space of this model. As $g_\mu - 2$ constraint pushes us to a region tilted towards large $\tan\beta$ with small m_A , it can lead to substantial branching fraction in the decay mode $h_{\text{SM}} \rightarrow AA$, when this particular decay is kinematically allowed, i.e., $m_A \lesssim \frac{m_h}{2}$. At large $\tan\beta$, pseudoscalar A decays to $\tau^+\tau^-$ pair with $\gtrsim 99\%$ branching fraction, leaving a small branching fraction ($\sim 0.35\%$) in the $\mu^+\mu^-$ final state [10,11,86,87]. LHC searches for $h_{\text{SM}} \rightarrow AA$ in the 4τ or $2\tau + 2\mu$ final state disfavors a large $\text{BR}(h_{\text{SM}} \rightarrow AA)$. We impose the most stringent upper limit $\text{BR}(h_{\text{SM}} \rightarrow AA) \lesssim 0.04$, consistent with the upper bounds provided by the experimental results [88].¹

First we consider scenario 1, i.e., $m_h = 125$ GeV. The partial decay width of Higgs decaying to a pair of pseudoscalars is given by

$$\Gamma(h \rightarrow AA) = \frac{1}{32\pi} \frac{g_{hAA}^2}{m_h} \sqrt{1 - 4m_A^2/m_h^2}. \quad (24)$$

Using the relations between the quartic couplings λ s and the physical masses and Higgs mixing parameter m_{12}^2 , in the alignment limit $|\sin(\beta - \alpha)| \approx 1$, hAA coupling [81] takes the following form.

$$g_{hAA} \propto (\lambda_3 + \lambda_4 - \lambda_5)v \approx \frac{\sin(\beta - \alpha)y_h^\ell(m_h^2 - m_H^2) + 2m_A^2 - m_{12}^2/(\sin\beta\cos\beta)}{v} \quad (25)$$

¹The limit is taken on the strongest side in our analysis. It may become slightly relaxed with varying m_A . Thus our study is conservative.

Expressing the quantity $y_h^\ell \sin(\beta - \alpha)$ in terms of g_{hAA} and mass parameters we get

$$y_h^\ell \sin(\beta - \alpha) = \frac{g_{hAA}v + m_{12}^2/(\sin\beta\cos\beta) - 2m_A^2}{m_h^2 - m_H^2}. \quad (26)$$

We can see from Eq. (24) that when $m_A \lesssim \frac{m_h}{2}$, the only way a small branching ratio for $\text{BR}(h \rightarrow AA)$ can be achieved is when the coupling g_{hAA} is extremely small. We should also remember from our discussion of perturbativity that, in this scenario $m_{12}^2 \approx \frac{m_\mu^2}{\tan\beta}$, in order to ensure perturbativity of the quartic couplings. If we demand perturbativity as well as the condition, $g_{hAA} \approx 0$, Eq. (26) implies $y_h^\ell \sin(\beta - \alpha) < 0$. In other words, wrong-sign lepton Yukawa coupling is more favored in scenario 1, when one demands smallness of $\text{BR}(h_{\text{SM}} \rightarrow AA)$ as well as perturbativity of the quartic couplings.

The other possibility is to consider the case when the heavier CP -even scalar is the SM-like Higgs, i.e., $m_H = 125$ GeV, which is our scenario 2. However, in this case the LEP limit implies either m_A or m_h can be less than $\frac{m_h}{2}$ [89]. We consider the low mass pseudoscalar and therefore $m_h > \frac{m_h}{2}$. Here the decay width of 125-GeV Higgs decaying to a pair of pseudoscalars is given by

$$\Gamma(H \rightarrow AA) = \frac{1}{32\pi} \frac{g_{HAA}^2}{m_h} \sqrt{1 - 4m_A^2/m_H^2}. \quad (27)$$

Here too, like the previous scenario, the limit on $\text{BR}(H \rightarrow AA)$ will indicate extremely small value of the coupling g_{HAA} , whose expression in the alignment limit, i.e., $|\cos(\beta - \alpha)| \approx 1$ is given as follows:

$$g_{HAA} \propto (\lambda_3 + \lambda_4 - \lambda_5)v \approx \frac{\cos(\beta - \alpha)y_H^\ell(m_H^2 - m_h^2) + 2m_A^2 - m_{12}^2/(\sin\beta\cos\beta)}{v}. \quad (28)$$

Expressing the quantity $y_H^\ell \cos(\beta - \alpha)$ in terms of g_{HAA} and mass parameters we get

$$y_H^\ell \cos(\beta - \alpha) = \frac{g_{HAA}v + m_{12}^2/(\sin\beta\cos\beta) - 2m_A^2}{m_H^2 - m_h^2}. \quad (29)$$

We can see from Eq. (29) that, as we are concerned with low pseudoscalar mass here ($m_A \lesssim \frac{m_h}{2}$), in the limit $g_{HAA} \approx 0$, $y_H^\ell \cos(\beta - \alpha)$ will be positive for the most part of our parameter space. Therefore we can conclude that the right-sign region will be favored in the case of scenario 2. We will see the implications of these in the next section.

Important limits come from the signal strength measurements of the 125-GeV Higgs in various final states including $\gamma\gamma$, ZZ , WW , $b\bar{b}$, and $\tau\tau$ final states [28,29]. The experimental data indicate that the gauge boson and Yukawa couplings of the 125-GeV scalar are very close to their SM value. Therefore in our analysis we confine ourselves to the alignment limit, i.e., $|y_{h/H}^V| \approx 1$ [$y_h^V = \sin(\beta - \alpha)$ for scenario 1 and $y_H^V = \cos(\beta - \alpha)$ for scenario 2] and $|y_{h/H}^e|$ is also close to unity. This in turn implies that $\tan\beta$ can not be very large in the RS region. However, in the WS region this condition gets slightly relaxed and $|y_{h/H}^V|$ can deviate slightly further from unity, within the allowed range and $\tan\beta$ can be large as long as $|y_{h/H}^e|$ is close to 1.

3. Direct search for heavier (pseudo)scalars at the LHC

Collider searches for the nonstandard neutral scalar states also put constraints on the parameter space of interest. Such searches are performed at the LHC, in various SM final states. As we are particularly interested in the low pseudoscalar mass region with its enhanced coupling to leptons, the limits which are crucial for our analyses, come from the search for low pseudoscalar produced in association with a pair of b quarks and decaying into $\tau\tau$ final state [90,91]. Constraints from the search for low mass (pseudo)scalar produced in association with $b\bar{b}$ and decaying into $b\bar{b}$ [92,93] have also been taken into account.

We have also taken into account the upper limits from CP -even nonstandard scalars (h/H) decaying to $\tau\tau$ [75] final state. CMS has also looked for decay involving two nonstandard Higgs bosons such as

$h/H \rightarrow AZ$ [94,95], $H \rightarrow hh$ [96–98], and $h/H \rightarrow VV$ [99–101].

At the LHC, the charged Higgs search can be produced in several ways. When $m_H^\pm < m_t$, charged Higgs can be produced from the decay of top quark ($t \rightarrow bH^\pm$). This decay has been searched for in $\tau\nu$ [102,103] and $c\bar{s}$ [104,105] final state. These searches put an upper limit on $\text{BR}(t \rightarrow bH^\pm) \times (H^\pm \rightarrow \tau\nu/c\bar{s})$. The other important search mode at the LHC is ($pp \rightarrow tbH^\pm$) in the final states $\tau\nu$ [103,106] and $c\bar{s}$ [107,108] and $t\bar{b}$ [109].

The most stringent bounds in the context of direct search for nonstandard scalars come from $pp \rightarrow h/H/A \rightarrow \tau\tau$ [91,110–112] and $pp \rightarrow tbH^\pm (H^\pm \rightarrow \tau\nu)$ [113]. Although in type-X model at large $\tan\beta$, the neutral nonstandard scalars decay to $\tau\tau$ with almost 100% BR and the charged Higgs decays to $\tau\nu$ final state almost exclusively, the production cross-section is suppressed at large $\tan\beta$ as the quark couplings scale as $1/\tan\beta$. This in turn puts a lower bound on $\tan\beta$ [75]. We would like to mention here that, although throughout the parameter space of our interest (typically large $\tan\beta$), $\text{BR}(H \rightarrow \tau\tau)$ or $\text{BR}(H^\pm \rightarrow \tau\nu)$ are almost 100%, the production cross section for these nonstandard scalar states are highly suppressed because of large $\tan\beta$. Therefore, the direct search constraints [90,91,102,110–113] do not put any significant bound on our parameter space. We have ensured that our chosen benchmarks are consistent with all the relevant experimental upper limits. In the figures showing constraints on the scenario, the aforesaid limits from direct search do not improve upon the stronger limits obtained from vacuum stability/perturbative unitarity/search based on $h_{\text{SM}} \rightarrow AA$ etc.

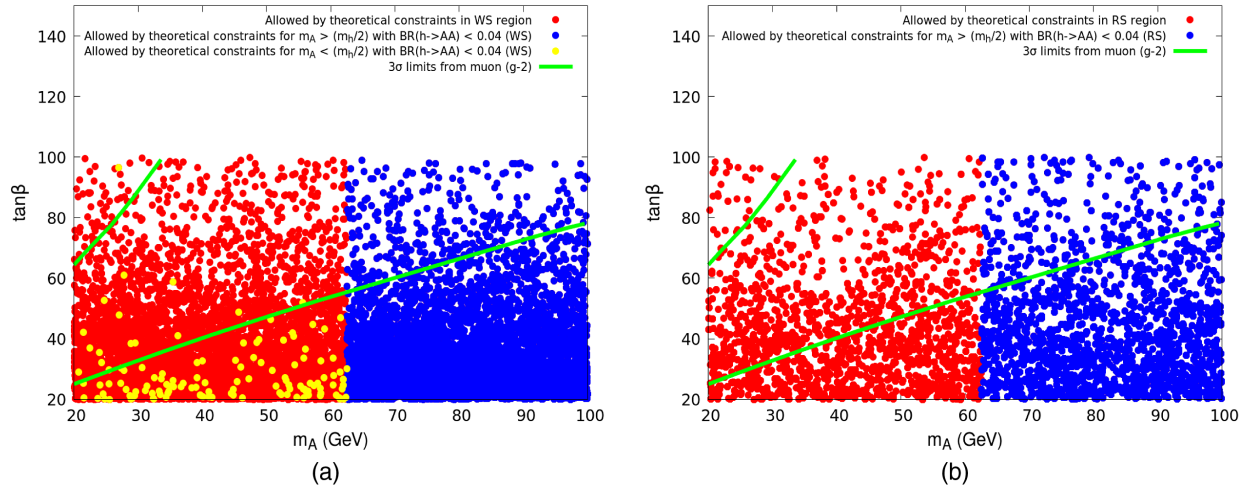


FIG. 8. Allowed parameter spaces in $m_A - \tan\beta$ plane for scenario 1 with (a) WS Yukawa and (b) RS Yukawa. The green lines denote the upper and lower limits coming from the observed $g_\mu - 2$ at 3σ level. All the points in the plots are allowed by theoretical constraints. Since perturbativity strongly constrains large $\tan\beta$ regions, we have chosen an upper limit for our scan $\tan\beta < 100$. $\tan\beta$ values beyond that are indeed allowed, subject to the constraints.

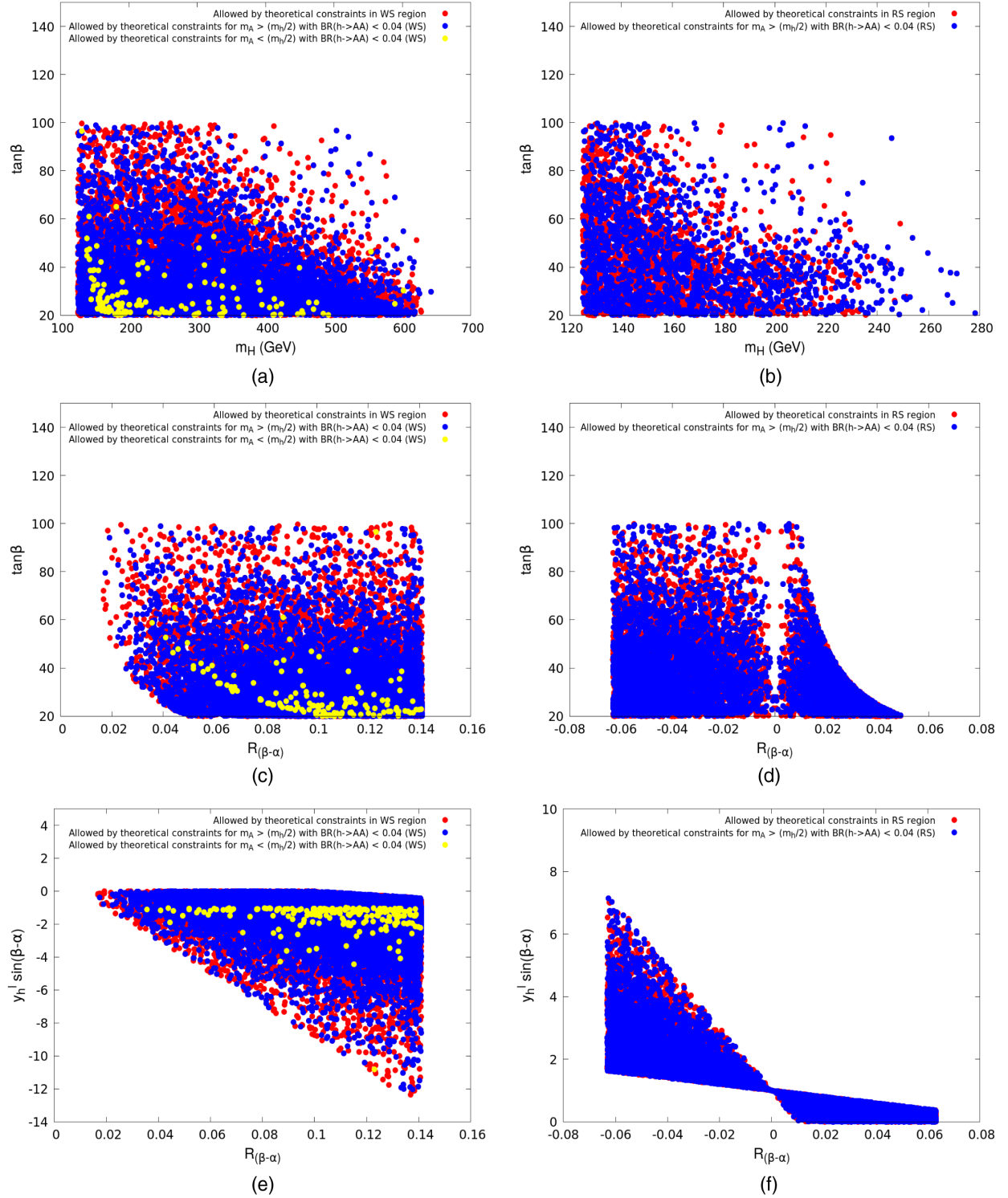


FIG. 9. Allowed parameter spaces in scenario 1 in (a) and (b) $m_H - \tan\beta$, (c) and (d) $R_{(\beta-\alpha)} - \tan\beta$, (e) and (f) $R_{(\beta-\alpha)} - y_h^c \sin(\beta - \alpha)$ plane. (a), (c), and (e) correspond to WS Yukawa; (b), (d), and (f) correspond to RS Yukawa. All the points in the plots are allowed by theoretical constraints. The explanation for upper limit on $\tan\beta$ is same as Fig. 8.

E. Allowed parameter space

Having listed all these constraints, our next task is to use them to constrain a type-X 2HDM, for both scenarios 1 and 2. We take this up in the present section.

Note that the parameter $\tan\beta$ has been varied up to 100 in our scan. Although one can in principle have higher values of $\tan\beta$. Such values get increasingly constrained due to reasons ranging from perturbativity

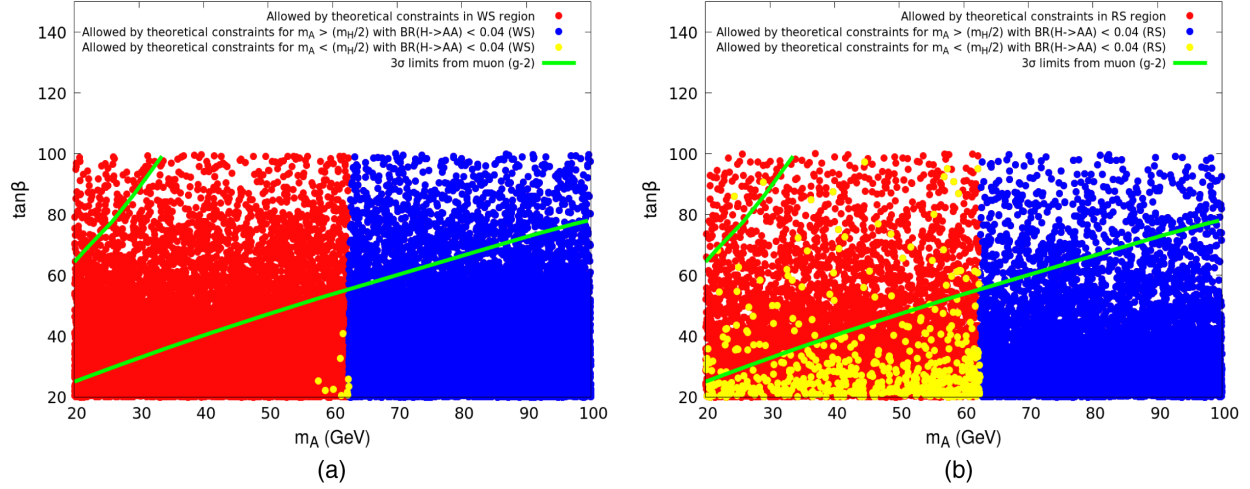


FIG. 10. Allowed parameter spaces in $m_A - \tan\beta$ plane for scenario 2 with (a) WS Yukawa and (b) RS Yukawa. The green lines denote the upper and lower limits coming from the observed $g_\mu - 2$. All the points in the plots are allowed by theoretical constraints. The explanation for upper limit on $\tan\beta$ is same as Fig. 8.

of τ Yukawa to enhancement of the $\tau\tau$ decay mode of light pseudoscalars.

1. Scenario 1

This scenario corresponds to the case, where lighter CP -even scalar is the SM-like Higgs boson. One can further categorize this scenario with WS and RS regions depending on the leptonic coupling of h , as discussed earlier. We scan our parameter space in the following ranges:

$$\begin{aligned} m_H &\in [125, 870] \text{ GeV}, & m_H^\pm &\in [125, 870] \text{ GeV}, \\ m_A &\in [20, 100] \text{ GeV}, & \tan\beta &\in [20, 100], \\ |\sin(\beta - \alpha)| &\in [0.99, 1], \\ m_{12}^2 &\in \left[\frac{m_H^2}{\tan\beta} - 200 \text{ GeV}^2, \frac{m_H^2}{\tan\beta} + 200 \text{ GeV}^2 \right]. \end{aligned} \quad (30)$$

We also mention here that $\lambda_6 = \lambda_7 = 0$, as we only consider soft Z_2 breaking terms.

In Fig. 8, we see that though theoretical constraints (namely, perturbativity, unitarity, and stability) prefer low to moderate $\tan\beta$, we can still get a large parameter space in WS domain which alleviates $g_\mu - 2$ discrepancy. On the other hand, in the RS region, large $\tan\beta$ is less favored. As discussed earlier in Sec. IV, we do not get a small enough $\text{BR}(h \rightarrow AA) \lesssim 4\%$ for $m_A \lesssim m_h/2$, as long as we are in the RS domain. This is clear from Fig. 8.

In Figs. 9(a) and 9(b), we show the allowed region in $m_H - \tan\beta$ plane. We can see that moderate $\tan\beta$ regions are favored by the theoretical constraints, especially when m_H is large. In addition to that, the upper bound from $\text{BR}(h_{\text{SM}} \rightarrow AA)$, pushes the allowed range of $\tan\beta$ to further lower side.

Figures 9(c) and 9(d) displays the allowed region in the $R_{(\beta-\alpha)} - \tan\beta$ plane, where $R_{(\beta-\alpha)}$ is defined as follows:

$$R_{(\beta-\alpha)} = \text{sgn}[\sin(\beta - \alpha)] \times \cos(\beta - \alpha). \quad (31)$$

On the whole, while the RS case admits $\sin(\beta - \alpha)$ with both signs, it is restricted to positive values only for WS. Furthermore, the WS picture disfavors large $\tan\beta$ from the limit on $\text{BR}(h_{\text{SM}} \rightarrow AA)$ so long as $m_A \lesssim \frac{m_h}{2}$.

In Figs. 9(e) and 9(f), we plot $y_h^\ell \times \sin(\beta - \alpha)$ against $R_{(\beta-\alpha)}$. The limit on $\text{BR}(h \rightarrow AA)$ for $m_A \lesssim m_h/2$ does not allow much deviation of $y_h^\ell \times \sin(\beta - \alpha)$ from unity, which is also consistent with the alignment limit. In Fig. 9(f), one can see that, both positive and negative signs for $\sin(\beta - \alpha)$ are equally consistent with the alignment limit ($|y_h^\ell \times \sin(\beta - \alpha)| \approx 1$) in the RS region.

2. Scenario 2

In this scenario, the heavier CP -even scalar H is the SM-like Higgs. To get the allowed regions in this scenario, we scan our parameter space in the following range:

$$\begin{aligned} m_h &\in [80, 125] \text{ GeV}, & m_H^\pm &\in [80, 180] \text{ GeV}, \\ m_A &\in [20, 100] \text{ GeV}, & \tan\beta &\in [20, 100], \\ |\cos(\beta - \alpha)| &\in [0.99, 1], \\ m_{12}^2 &\in \left[\frac{m_H^2}{\tan\beta} - 200 \text{ GeV}^2, \frac{m_H^2}{\tan\beta} + 200 \text{ GeV}^2 \right]. \end{aligned} \quad (32)$$

In Figs. 10 and 11, we plot the points allowed by theoretical constraints as well as constraints on $\text{BR}(H \rightarrow AA)$, in two-dimensional planes of various model parameters.

If we focus on Fig. 10(a), then it becomes clear that for $m_A \lesssim \frac{m_h}{2}$, the constraints on HAA coupling can leave a very narrow region near resonance $m_A \approx m_H/2$, for WS cases, which is not quite compatible with the $g_\mu - 2$ observation, within 3σ . But the situation will be more relaxed in the RS

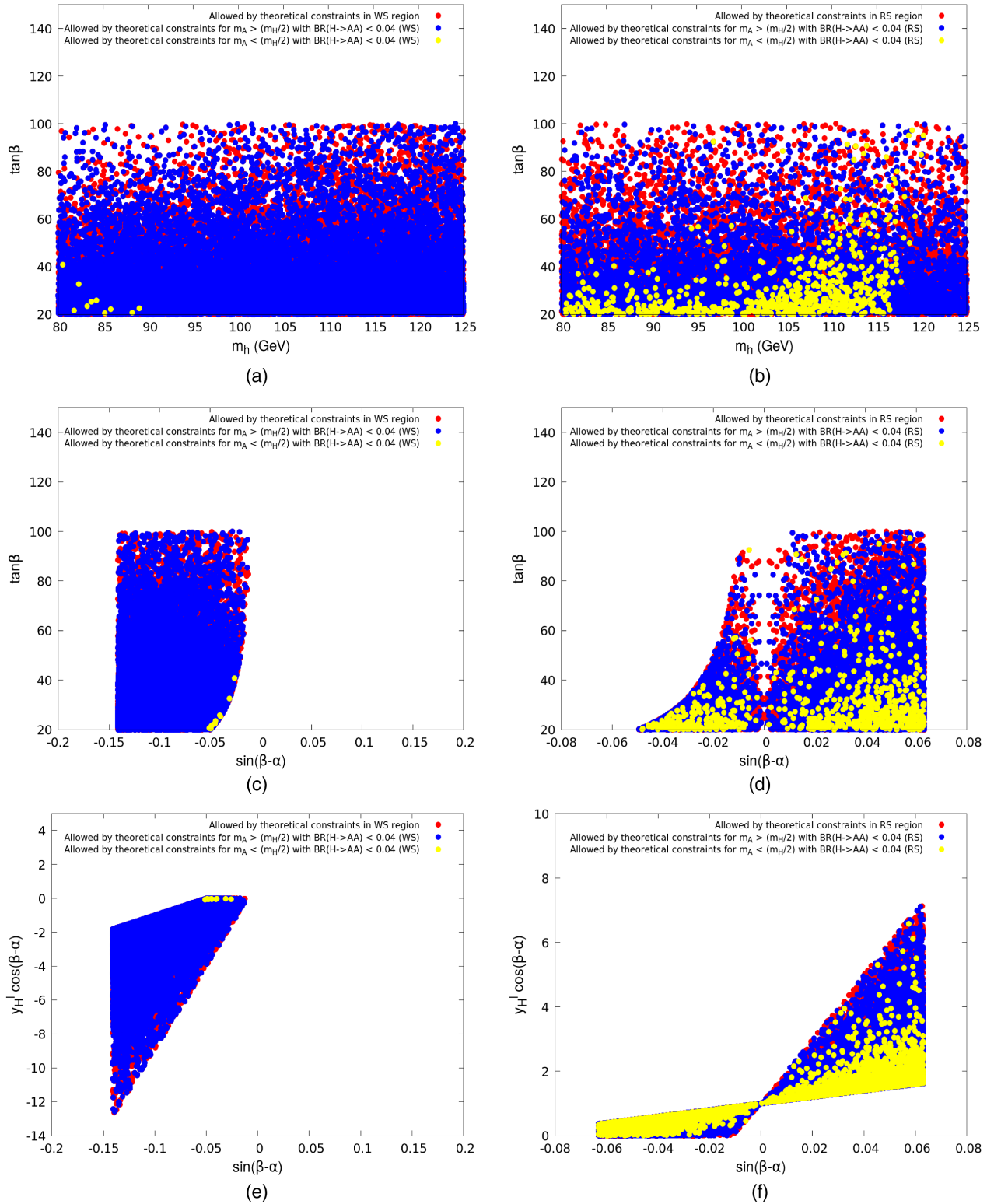


FIG. 11. Allowed parameter spaces in scenario 2 in (a) and (b) $m_H - \tan\beta$, (c) and (d) $\sin(\beta - \alpha) - \tan\beta$, (e) and (f) $\sin(\beta - \alpha) - y_h^\ell \times \sin(\beta - \alpha)$ plane. (a), (c), and (e) correspond to WS Yukawa; (b), (d), and (f) correspond to RS Yukawa. All the points in the plots are allowed by theoretical constraints. The explanation for upper limit on $\tan\beta$ is same as Fig. 8.

domain for scenario 2 [yellow points in Fig. 10(b)]. On the other hand, we can get a large parameter space both in WS and RS region, which can solve $g_\mu - 2$ discrepancy, for $m_A > \frac{m_H}{2}$.

In Figs. 11(a) and 11(b), the allowed regions in $m_h - \tan\beta$ plane are shown for the WS and RS, respectively. We can see that, in the RS case, low to moderate $\tan\beta$ will be favored from the requirement of low $\text{BR}(h_{\text{SM}} \rightarrow AA)$. However, when the difference between the lighter and heavier CP -even scalar masses decreases, even larger $\tan\beta$ becomes allowed.

In Figs. 11(c) and 11(d), we show the allowed region in $\sin(\beta - \alpha) - \tan\beta$ plane where both positive and negative $\sin(\beta - \alpha)$ is allowed for RS cases, but WS is attained with only negative $\sin(\beta - \alpha)$.

In Figs. 11(e) and 11(f), one can see similar behavior as scenario 1, where small $\text{BR}(H \rightarrow AA)$ for $m_A \lesssim \frac{m_H}{2}$ prefers lepton Yukawa coupling y_h^ℓ close to unity, consistent with the observed Higgs signals for both WS and RS cases.

V. THE RUNNING OF VARIOUS COUPLINGS

A. The RGEs

The parameters constrained above are considered at the electroweak scale, set at the pole mass of top quark (~ 173.34 GeV). We now investigate how they evolve at higher scales and thus obtain their domain of validity in the light of vacuum stability (following [80]) and perturbative unitarity (following [78]). This yields the cutoff scale $\Lambda_{\text{UV}}^{\text{cutoff}}$, which precludes the vitiation of the RG-evolution trajectories via the occurrence of Landau pole.

In this subsection, we present the one-loop RG equations for the various quartic couplings as well as the gauge and third generation Yukawa couplings. For the actual presentation of our results, we will take recourse to the two-loop renormalization group equations [114] for enhanced precision and rigor. However, we will soon see that, qualitatively the evolution trajectories at the one- and two-loop levels are very similar in our case and that the quantitative differences are rather minor, at least at energy scales well below the perturbative limits of couplings. Keeping this in view, we start by presenting the one-loop RGEs so that we can fall back on them to provide intuitive explanations of the trajectories. At the same time, the detailed results presented in the next subsection are all based on two-loop equations, although we take the liberty of explaining them in terms of one-loop equations, empowered by reasons summarized above.

First, we present the one-loop RGEs for the gauge couplings.

$$\begin{aligned} 16\pi^2\beta_{g_1} &= 7g_1^3, \\ 16\pi^2\beta_{g_2} &= -3g_2^3, \\ 16\pi^2\beta_{g_3} &= -7g_3^3. \end{aligned} \quad (33)$$

They form a stand-alone set, at one loop, as we can see from Eq. (33), and therefore they remain unchanged for different types of 2HDMs. We mention here that, in writing Eq. (33), GUT normalization has not been used.

We focus next on the RGE of the Yukawa couplings in type-X 2HDM. The corresponding equations are as follows. Here g and Y in the superscripts, respectively, denote gauge and Yukawa interactions, contributing to the running of the Yukawa couplings (taken here as real).

$$\begin{aligned} 16\pi^2\beta_{Y_t}^g &= -\left(\frac{17}{12}g_1^2 + \frac{9}{4}g_2^2 + 8g_3^2\right)Y_t, \\ 16\pi^2\beta_{Y_t}^Y &= \left(\frac{3}{2}Y_b^2 + \frac{9}{2}Y_t^2\right)Y_t, \\ 16\pi^2\beta_{Y_b}^g &= -\left(\frac{5}{12}g_1^2 + \frac{9}{4}g_2^2 + 8g_3^2\right)Y_b, \\ 16\pi^2\beta_{Y_b}^Y &= \left(\frac{9}{2}Y_b^2 + \frac{3}{2}Y_t^2\right)Y_b, \\ 16\pi^2\beta_{Y_\tau}^g &= -\left(\frac{15}{4}g_1^2 + \frac{9}{4}g_2^2\right)Y_\tau, \\ 16\pi^2\beta_{Y_\tau}^Y &= \frac{5}{2}Y_\tau^3. \end{aligned} \quad (34)$$

The resulting beta function will be the sum of the gauge and Yukawa components.

$$\beta_Y = \beta_Y^g + \beta_Y^Y. \quad (35)$$

The Yukawa and gauge contributions show similar behavior for Y_t and Y_b . It is clear from Eq. (34) that the gauge contribution decreases with energy whereas the Yukawa part goes up at higher energy. However, the terms involving the strong coupling constant g_3 dominates over the other terms and therefore the top and bottom Yukawa couplings monotonically decrease with energy. The τ -Yukawa coupling on the other hand, unaffected by the strong interaction, remains almost constant. This behavior can be seen in Fig. 15.

The relevant equations for the running of quartic couplings are given below. Here, the superscripts b and Y denote, respectively, bosonic (gauge couplings and quartic couplings) and Yukawa interactions, contributing to the running of λ s.

$$\begin{aligned} 16\pi^2\beta_{\lambda_1}^b &= \frac{3}{4}g_1^4 + \frac{3}{2}g_1^2g_2^2 + \frac{9}{4}g_2^4 - 3g_1^2\lambda_1 - 9g_2^2\lambda_1 + 12\lambda_1^2 \\ &\quad + 4\lambda_3^2 + 4\lambda_3\lambda_4 + 2\lambda_4^2 + 2\lambda_5^2, \\ 16\pi^2\beta_{\lambda_1}^Y &= -4Y_\tau^4 + 4Y_\tau^2\lambda_1, \\ 16\pi^2\beta_{\lambda_2}^b &= \frac{3}{4}g_1^4 + \frac{3}{2}g_1^2g_2^2 + \frac{9}{4}g_2^4 - 3g_1^2\lambda_2 - 9g_2^2\lambda_2 + 12\lambda_2^2 \\ &\quad + 4\lambda_3^2 + 4\lambda_3\lambda_4 + 2\lambda_4^2 + 2\lambda_5^2, \\ 16\pi^2\beta_{\lambda_2}^Y &= -12Y_b^4 - 12Y_t^4 + (12Y_b^2 + 12Y_t^2)\lambda_2, \end{aligned}$$

$$\begin{aligned}
 16\pi^2\beta_{\lambda_3}^b &= \frac{3}{4}g_1^4 - \frac{3}{2}g_1^2g_2^2 + \frac{9}{4}g_2^4 - 3g_1^2\lambda_3 - 9g_2^2\lambda_3 \\
 &\quad + (\lambda_1 + \lambda_2)(6\lambda_3 + 2\lambda_4) + 4\lambda_3^2 + 2\lambda_4^2 + 2\lambda_5^2, \\
 16\pi^2\beta_{\lambda_3}^Y &= (6Y_b^2 + 6Y_t^2 + 2Y_\tau^2)\lambda_3, \\
 16\pi^2\beta_{\lambda_4}^b &= 3g_1^2g_2^2 - (3g_1^2 + 9g_2^2)\lambda_4 + 2\lambda_1\lambda_4 + 2\lambda_2\lambda_4 \\
 &\quad + 8\lambda_3\lambda_4 + 4\lambda_4^2 + 8\lambda_5^2, \\
 16\pi^2\beta_{\lambda_4}^Y &= (6Y_b^2 + 6Y_t^2 + 2Y_\tau^2)\lambda_4, \\
 16\pi^2\beta_{\lambda_5}^b &= (-3g_1^2 - 9g_2^2 + 2\lambda_1 + 2\lambda_2 + 8\lambda_3 + 12\lambda_4)\lambda_5, \\
 16\pi^2\beta_{\lambda_5}^Y &= (6Y_b^2 + 6Y_t^2 + 2Y_\tau^2)\lambda_5. \tag{36}
 \end{aligned}$$

Like before, the actual beta function will be the sum of the bosonic and Yukawa components:

$$\beta_\lambda = \beta_\lambda^b + \beta_\lambda^Y. \tag{37}$$

One should note, since the Yukawa couplings depend on the specific kinds of 2HDM, it is obvious that their evolution as well as those of the quartic couplings are model dependent. This is obvious from Eqs. (34) and (36).

B. Coupling trajectories and inference drawn from them

In this subsection, the running of various couplings will be illustrated in terms of a few chosen benchmark points. A brief justification for choosing those will be given shortly. Based on the discussion in the preceding subsection, we will present here the full two-loop results for our benchmark points (BPs). Our chosen benchmarks are consistent with theoretical as well as experimental constraints.

We have seen that, in scenario 1, the requirement of a low branching fraction of SM-like Higgs to two pseudoscalars along with other constraints leads us to $m_A > \frac{m_h}{2}$ in the RS region. However, it is possible to get allowed points in the whole range of m_A in the WS regime. Keeping this in mind, we choose three benchmarks BP1, BP2, and BP3 for scenario 1. BP1 corresponds to WS region with $m_A > \frac{m_h}{2}$. BP2 corresponds to WS region and $m_A < \frac{m_h}{2}$. For BP3, we have taken RS with $m_A > \frac{m_h}{2}$. We present the benchmark points chosen for scenario 1 in Table II.

As long as we are in the alignment limit with large $\tan\beta$, λ_2 is precisely determined by SM-like Higgs with a very small value ($\approx \frac{m_h^2}{v^2} \approx 0.258$), which is the case for all the benchmarks in Table II. On the other hand, λ_1 and λ_3 depend on the mass splitting between two CP -even scalars. Furthermore, λ_1 can be controlled by m_{12}^2 , which gets an enhancement factor in the large $\tan\beta$ region. As for this parameter space, we have $m_{12}^2 \sim \frac{m_h^2}{\tan\beta}$ with large $\tan\beta$, λ_4 is proportional to $m_A^2 - 2m_{H^\pm}^2 + m_H^2$ and takes a negative value for our benchmarks. Similarly, λ_5 takes a value close to λ_4 with a opposite sign, being proportional to

TABLE II. Benchmark points for scenario 1.

	BP1	BP2	BP3
m_H in GeV	449.734	324.237	153.865
m_A in GeV	80.0	24.6997	63.0
m_{H^\pm} in GeV	453.895	331.34	176.152
λ_1	0.095392	1.4963	0.52616
λ_2	0.25788	0.25792	0.25773
λ_3	6.9130	3.5968	0.52559
λ_4	-3.3549	-1.8783	-0.56774
λ_5	3.23062	1.72343	0.324993
m_{12}^2 in GeV ²	2696.2389	1992.85	353.226215
$\tan\beta$	75.0	52.7154	67.0
$\sin(\beta - \alpha)$	0.9996	0.999163	0.999996
$y_h^\ell \times \sin(\beta - \alpha)$	-1.12095144	-1.15624366	0.81048833
Δa_μ	84.59×10^{-11}	234.65×10^{-11}	82.28×10^{-11}

$-m_A^2 + m_H^2$. It is clearly seen that for degenerate m_H and m_{H^\pm} , $\lambda_5 \approx -\lambda_4$. The equality in magnitude is prominent in case of large m_H . For BP3 this does not apply. However, the mutual opposite sign between λ_4 and λ_5 still holds. We would like to mention here that all the benchmarks satisfy the limit on y_h^ℓ as well as y_h^V from the alignment condition [28,29].

In Fig. 12, we can see the two-loop RG running of quartic couplings for BP1, BP2, and BP3. For all these benchmarks tree level unitarity decides the value of $\Lambda_{UV}^{\text{cutoff}}$ which is denoted by the end scale in all figures, whereas stability and perturbativity can be satisfied even after that cutoff scale. It is clear from the running that the larger the value for any quartic coupling at the electroweak scale, the quicker it breaks the unitarity criteria. For both BP1 and BP2, λ_3 becomes the largest among the quartic couplings at the breakdown scale, whereas in BP3 λ_1 plays this role. Also from Fig. 12(c), it is clear that starting from nearly the same value, λ_1 can increase faster than λ_3 as energy increases. On the other hand, the runnings of other λ s show a flat nature compared to λ_1 and λ_3 . As we do not allow hard Z_2 breaking, λ_6 and λ_7 do not change with energy and are fixed at zero. In explicit terms, the RG equations for λ_6 and λ_7 , always carry the terms proportional to these two λ s and therefore the relation $\frac{d\lambda}{d\mu} = 0$ remains valid throughout their running.

A complementary picture is noticed in scenario 2. Here the requirement of a low branching fraction of SM-like Higgs to a pair of pseudoscalars along with other constraints pushes $m_A > \frac{m_h}{2}$ in the WS region. On the other hand, in the RS case, it is possible to get a low $\text{BR}(h_{\text{SM}} \rightarrow AA)$ in the entire range of m_A . To examine scenario 2 on a case by case basis, we choose three benchmarks BP4, BP5, and BP6. BP4 corresponds to the RS region with $m_A > \frac{m_h}{2}$, BP5 corresponds to the RS region with $m_A < \frac{m_h}{2}$. We consider WS region with $m_A > \frac{m_h}{2}$ in BP6. The benchmarks for scenario 2 are listed in Table III. We mention here that

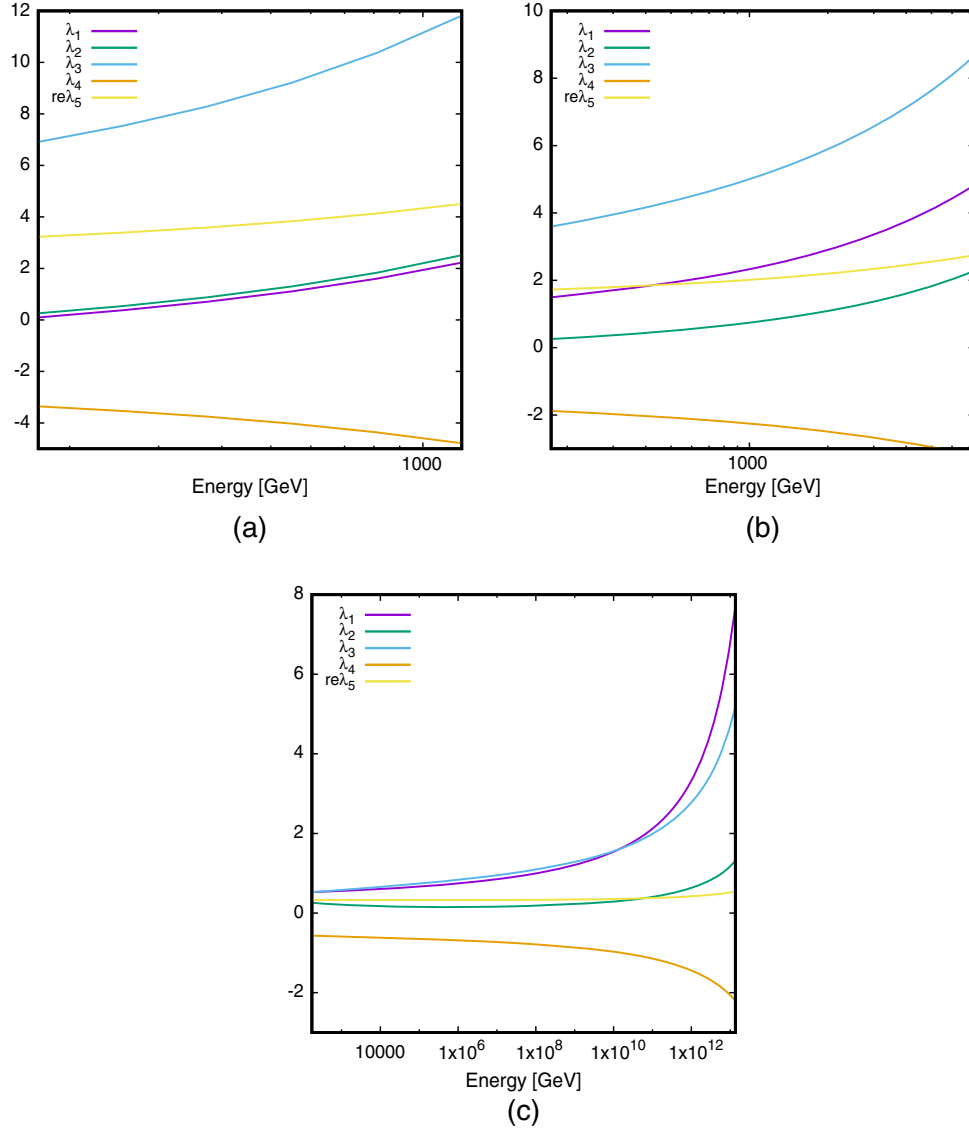


FIG. 12. Two-loop RG running of quartic couplings for the benchmarks (a) BP1 (WS), (b) BP2 (WS), and (c) BP3 (RS) from scenario 1.

although it is possible to get a few points in the WS region, with $m_A \lesssim \frac{m_H}{2}$, in the resonant region with severe fine-tuning, we do not consider this region further in our analysis.

Our BP4 and BP6 have negative $\sin(\beta - \alpha)$ and large $\tan\beta$, where BP5 has positive $\sin(\beta - \alpha)$ and comparatively small $\tan\beta$. Here too, in the alignment limit, λ_2 is governed by the 125-GeV Higgs mass and therefore for all the benchmarks, its values remain similar to that in scenario 1. In this case, λ_3 is comparatively smaller than the previous case due to smaller mass gap between m_H and m_h , whereas λ_1 can get a somewhat enhanced contribution from the m_{12}^2 term at large $\tan\beta$. On the other hand, λ_4 and λ_5 are opposite in sign, similar to the previous scenario.

Having thus identified our benchmark points, we further note that all the six aforesaid benchmark points fall in the

TABLE III. Benchmark points for scenario 2.

	BP4	BP5	BP6
m_H in GeV	117.409	93.6073	121.446
m_A in GeV	67.0	15.7859	64.0
m_{H^\pm} in GeV	167.0	135.00	171.0
λ_1	0.013324	1.0251	0.060649
λ_2	0.25774	0.25767	0.25773
λ_3	0.71998	0.58636	0.70471
λ_4	-0.61858	-0.45412	-0.65377
λ_5	0.153385	0.138905	0.175768
m_{12}^2 in GeV^2	196.928761	393.28757	216.89098
$\tan\beta$	70.0	22.0	68.00
$\sin(\beta - \alpha)$	-0.00141421	0.00601127	-0.03161882
$y_h^e \times \cos(\beta - \alpha)$	0.901003399	1.13220955	-1.14940501
Δa_μ	132.17×10^{-11}	69.67×10^{-11}	121.83×10^{-11}

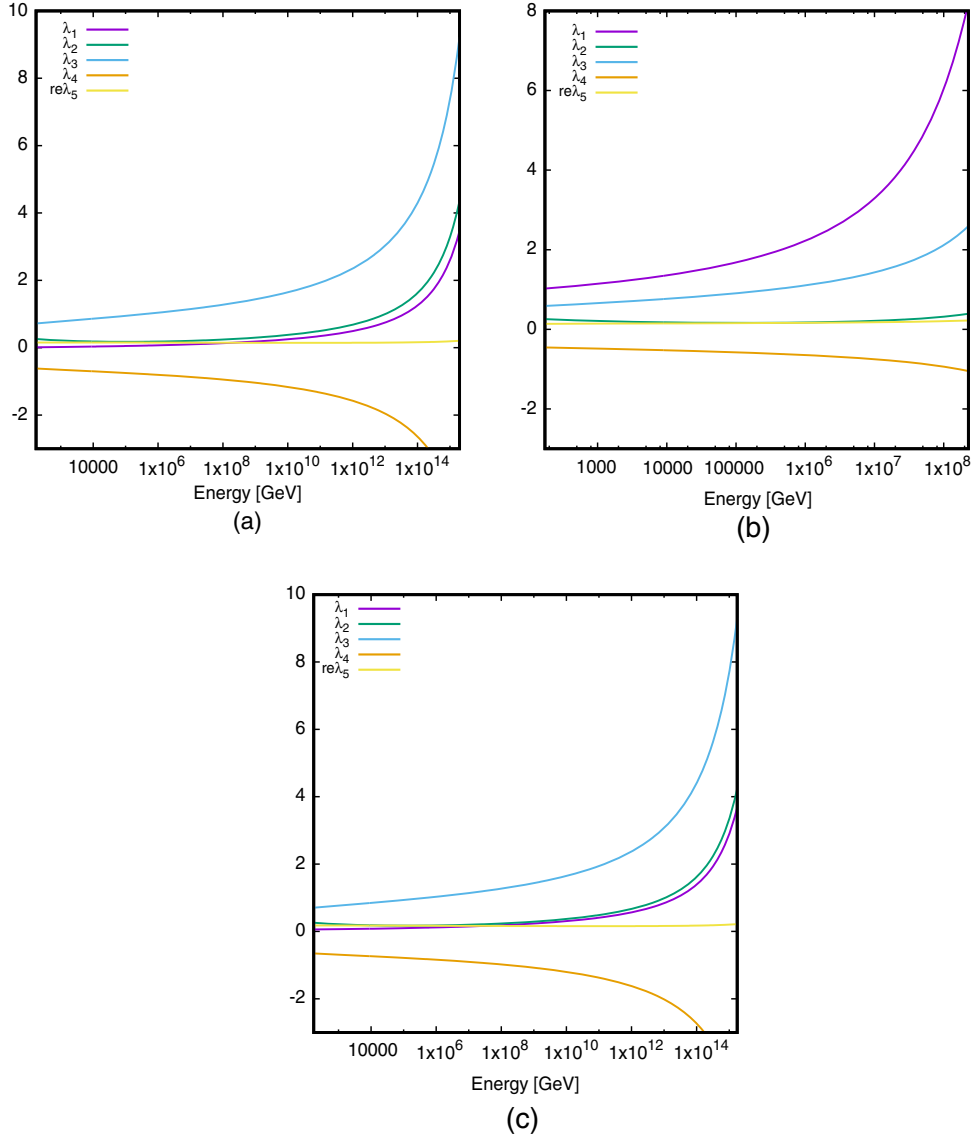


FIG. 13. Two-loop RG running of quartic couplings for the benchmarks (a) BP4 (RS), (b) BP5 (RS), and (c) BP6 (WS) from scenario 2.

yellowish interior region of Fig. 5. Therefore our analyses based on them are legitimate, both with the older data and on taking the very recent results into account, as far as constraints from $g_\mu - 2$ are concerned. For our subsequent analysis on UV completion, we shall use the combined data of $g_\mu - 2$ as the constraining factor on the parameter space.

In Fig. 13, we display two-loop RG running of quartic couplings for BP4, BP5, and BP6. We can see that for all the three benchmarks $\Lambda_{\text{UV}}^{\text{cutoff}}$ is again decided by tree-level unitarity. For BP4 and BP6, comparatively smaller values of λ_s at the electroweak scale ensure tree-level unitarity as well as perturbativity and stability up to a very high scale ($\sim 10^{16}$ GeV). We can see that in general, it is easier to achieve UV completion for scenario 2 than 1.

We have noticed in Figs. 12 and 13 that for all the λ_s , the negative contribution to the running of λ_s comes from the combination $(3g_1^2 + 9g_2^2)\lambda$ and terms involving Yukawa couplings. If to this we couple the information that g_2 falls at higher energies, while g_1 has at best marginal rise and the Yukawa couplings remain more or less constant, one finally has all quartic couplings rising with energy in this scenario. This feature, which is generic to 2HDMs, is due to the proliferation of bosonic degrees of freedom in the RG equations. Thus the stronger constraint almost invariably comes from perturbative unitarity.

The quartic coupling λ_2 shows a unique behavior. For some benchmarks (namely BP1 and BP2) it shows the usual monotonically increasing trend. But for the other BPs (BP3 to BP6), it decreases initially and then increases. The reason behind this behavior is the following: in the case of

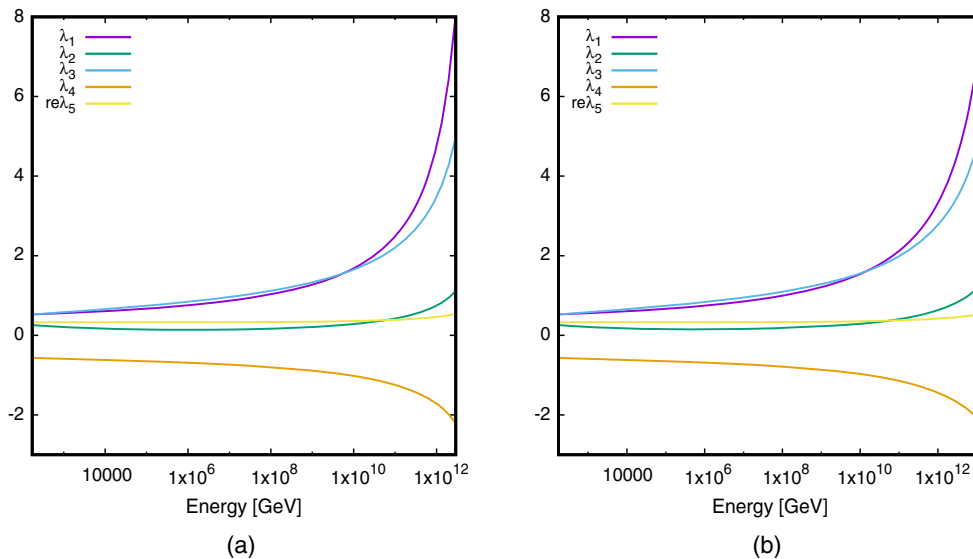


FIG. 14. (a) One-loop and (b) two-loop RG running of quartic couplings for BP3 (RS) from scenario 1.

BP1 and BP2, the magnitude of λ_3 , λ_4 , and λ_5 are much larger compared to the rest of the benchmarks. The terms proportional to λ_3 , λ_4 , and λ_5 control the positive contribution to the beta function for λ_2 . Therefore depending on their values the cancellation between the positive and negative terms can sometimes, take place. However, here the dominant negative contribution comes from terms involving Yukawa couplings and their strengths drop at higher energies. Thus λ_2 starts to increase at high energies for all the benchmarks. One can also note that this behavior is correlated to the mass difference between the two neutral scalars h and H as the coupling λ_3 is proportional to this mass difference. It is evident from Table II that, in the case of BP1 and BP2, this mass difference is much larger. Consequently, the beta function for λ_2 takes a positive value in these cases at all energies.

On the other hand, in the case of BP3, we see that λ_1 and λ_3 start from similar low energy values, but λ_1 tends to grow faster. As in this case $\lambda_1, \lambda_3 > \lambda_2, \lambda_4$, the bosonic contribution is larger in the case of λ_1 compared to λ_3 . The Yukawa contributions drop with energy whereas the bosonic contributions keep growing. Therefore, beyond a certain energy ($\sim 10^{10}$ GeV), λ_1 becomes larger than λ_3 .

Another interesting feature can be observed if we compare the running of λ_4 and λ_5 in the case of BP1 and BP2. In these two cases, at the EW scale, $|\lambda_4| \approx |\lambda_5|$ as can be seen from Table II. It can be checked from Eq. (36) that, in this limit, the beta functions for λ_4 and λ_5 become almost equal to each other in magnitude and opposite in sign. This behavior is clearly seen in Fig. 12.

A comparison has been made between one-loop and two-loop RG running of quartic couplings in Fig. 14, for a representative benchmark (BP3). We have seen that in the case of one-loop RG evolution unitarity breaks down faster than in the two-loop case. However, the breaking scale is of

the order of 10^{13} GeV in both cases. The values of quartic couplings, too, are very similar at high scales. Nonetheless, it is seen that the two-loop contribution helps us achieve somewhat higher UV cutoff scales.

The running of the gauge and Yukawa couplings are shown in the case of BP3 and BP4 in Fig. 15. The qualitative nature of the running will be the same for all the benchmarks. The variation in the top- and bottom-Yukawa couplings are significant, as can be seen through the logarithmic plots, since they are affected by strong interaction, unlike what happens to the τ Yukawa [see Eq. (34)]. The τ -Yukawa interaction overrides even the top-Yukawa coupling at high scales, by virtue of the fact that we are considering benchmark points with large $\tan\beta$.

Some remarks are in order on the evolution of the gauge couplings, especially in the context of possible embedding of the type-X 2HDM in a GUT. As far as the gauge interactions are concerned, the evolution patterns are largely similar to the SM trajectories, if one remembers that GUT normalization has not been used for the U(1) gauge coupling. It should also be noted that one loses perturbative unitarity of quartic couplings at around 10^{13} GeV for BP3, and even the two-loop RGEs cease to be trustworthy beyond that. So long as perturbativity is held to be sacrosanct, one therefore needs the intervention of new physics within approximately 10^{13} GeV in this case, and that intervening physics should have a role in ensuring grand unification, if at all. For BP4, on the other hand, no such requirement arises since the interactions are perturbative almost all the way to the GUT scale. However, the merger of the three kinds of gauge interaction at the GUT scale still requires some additional threshold effects, as much as they do in the standard model, a requirement eminently fulfilled, for example, by supersymmetry broken at the TeV scale.

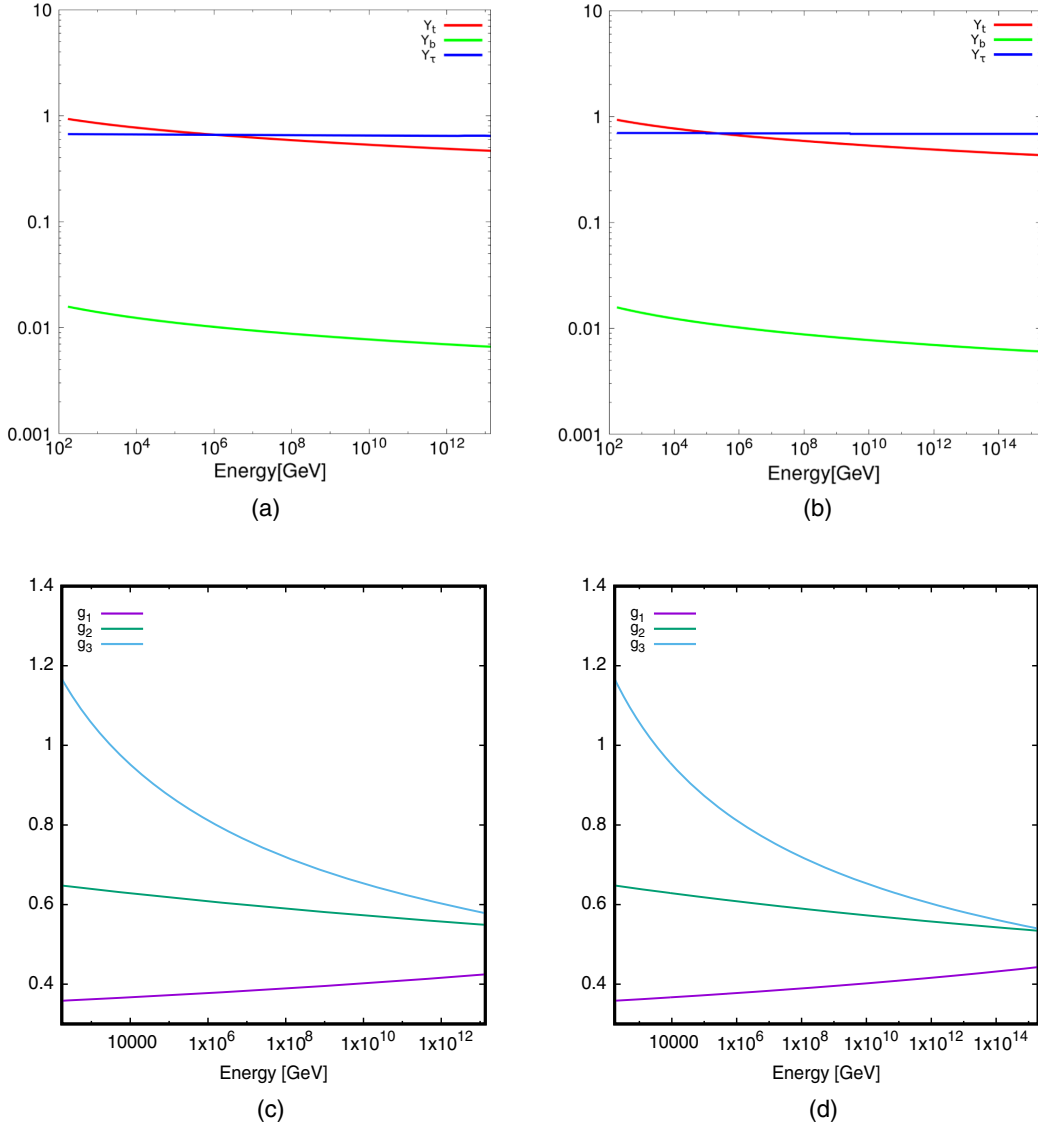


FIG. 15. Two-loop RG running of third generation Yukawa couplings for (a) BP3 (RS scenario 1) and (b) BP4 (RS scenario 2) and gauge couplings for (c) BP3 (RS scenario 1) and (d) BP4 (RS scenario 2), respectively.

VI. ALLOWED REGIONS WITH VARIOUS CUTOFF SCALES

After discussing the RG evolutions of all the relevant couplings in the model, we proceed to scan the model parameter space and look for points that satisfy all the theoretical constraints, namely perturbativity, unitarity, and vacuum stability up to cutoff scale $\Lambda_{\text{UV}}^{\text{cutoff}}$. Four values of such scale, have been used as benchmarks here. These are $\sim 10^4, 10^8, 10^{16}$, and 10^{19} GeV. While the last two are connected with the GUT and Planck scales, we have also thought in terms of intermediate scales such as 10^8 GeV. Lastly, $\Lambda_{\text{UV}}^{\text{cutoff}} \sim 10^4$ GeV, too, has been included in the study, which corresponds to a situation where, a rather rich intermediate sector becomes obvious with potential implications in collider phenomenology. To maintain consistency

in the discussion we divide our analysis in four previously considered scenarios namely

- (1) Case 1: Scenario 1 with WS Yukawa.
- (2) Case 2: Scenario 1 with RS Yukawa.
- (3) Case 3: Scenario 2 with WS Yukawa.
- (4) Case 4: Scenario 2 with RS Yukawa.

We will identify the allowed parameter spaces for each of these cases in two-dimensional planes of relevant physical model parameters as well as the quartic couplings λ s. In all the plots in Figs. 16–27 the blue, green, red, and yellow points represent the regions valid up to $10^4, 10^8, 10^{16}, 10^{19}$ GeV, respectively.

A. Case 1

In Fig. 16(a), the two black lines represent the upper and lower bounds from $g_\mu - 2$ anomaly at 3σ . Figure 16(b)

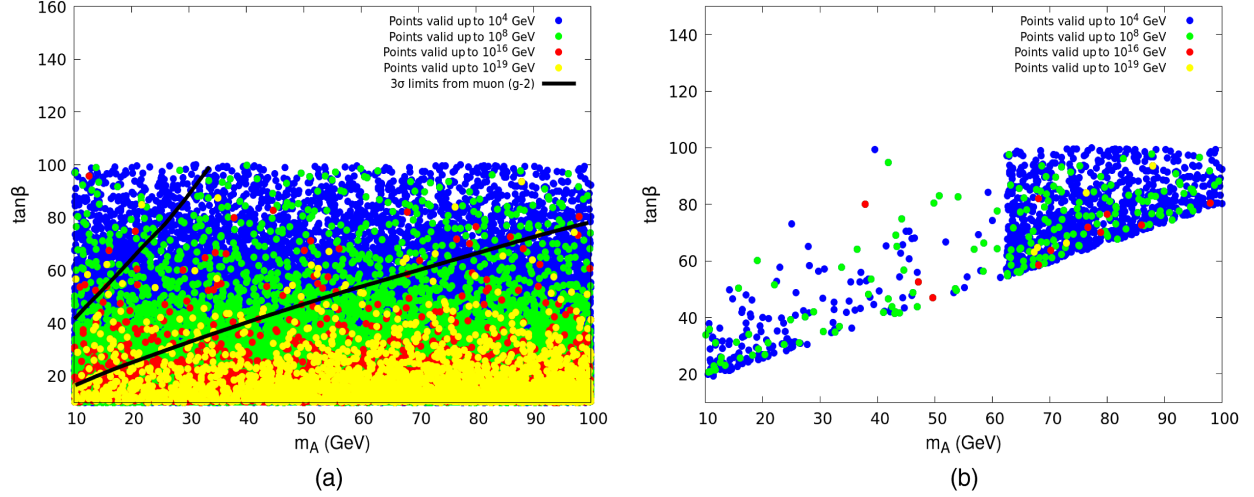


FIG. 16. $m_A - \tan\beta$ plane, valid up to different energy scales after applying (a) theoretical constraints (b) theoretical constraints $+ (g_\mu - 2)$ at $3\sigma + \text{BR}(h_{\text{SM}} \rightarrow AA)$ bounds for case 1.

shows the allowed parameter space which satisfy the observed $g_\mu - 2$ as well as the strong upper limit from $\text{BR}(h_{\text{SM}} \rightarrow AA)$. It can be seen from this plot that high-scale validity up to the Planck scale favors $\tan\beta \lesssim 30$. At the electroweak scale, we have seen that large $\tan\beta$ regions are disfavored from the requirement of perturbative unitarity, since large $\tan\beta$ eventually results in large λ_s . For high-scale validity, λ_s need to be small at the electroweak scale. Naturally, relatively small values of $\tan\beta$ are favored from the standpoint of high-scale validity. On the other hand, the observed $g_\mu - 2$ prefers $\tan\beta$ on the higher side, rendering a very tiny region valid up to the Planck scale, which is clear from Fig. 16(b). In the same figure, we see a sharp discontinuity in the allowed parameter space around $m_A \approx m_h/2$. This is because of the fact that when $m_A \lesssim \frac{m_h}{2}$, one is strongly restricted by the limit $\text{BR}(h_{\text{SM}} \rightarrow AA) \lesssim 4\%$. This constraint is particularly severe for large $\tan\beta$, a feature we have already seen in Sec. IV.

In Figs. 17(a)–17(c), we show the high-scale validity in the $(m_H - \tan\beta)$, $(\sin(\beta - \alpha) - \tan\beta)$, and $(m_H - m_{H^\pm})$ planes, respectively. We can see that the high-scale validity demands smaller m_H . The major reason behind this is the following. As λ_3 increases with m_H in this region [see Eq. (17)], the requirement of small λ_3 at the electroweak scale (which is necessary for high-scale validity) pushes us towards small m_H values. One more feature from the figure is that, when $\tan\beta \lesssim 50$, there is a discontinuity in the allowed points. The reason behind this is the following. The parameter space with $\tan\beta \lesssim 50$ and $m_A > \frac{m_h}{2}$, albeit allowed by the $\text{BR}(h_{\text{SM}} \rightarrow AA)$ constraints, faces severe constraint from the lower limit on $(g_\mu - 2)$ [see Fig. 16(a)]. On the other hand, the small strip below $\tan\beta \lesssim 50$ corresponds to the points where $m_A \lesssim \frac{m_h}{2}$ and $\text{BR}(h_{\text{SM}} \rightarrow AA)$ upper limit is satisfied. Similar feature is

observed in Fig. 17(b) where the small strip below $\tan\beta \lesssim 50$ corresponds to $m_A \lesssim \frac{m_h}{2}$. From Fig. 17(c), we can see that the high-scale validity puts a strong upper bound on m_H , which also follows from our understanding of the perturbativity and unitarity condition at the electroweak scale. The degeneracy between m_H and m_{H^\pm} mass naturally pushes the charged scalar mass to smaller values, at the high scales, which is evident from Fig. 17(c).

Let us now discuss the high-scale validity in the planes spanned by the quartic couplings, as they play the key role in this regard. In Fig. 18(a), we can see that λ_1 controls the high-scale behavior much more than λ_2 . This happens because λ_2 at the electroweak scale is solely determined by the 125-GeV Higgs mass and varies only slightly with energy, a behavior we have already seen. With the variation in scale from 10^4 to 10^{19} GeV, the allowed range of λ_2 varies only slightly around its electroweak value. On the contrary, allowed range for λ_1 varies from 3 to 0.5 with the same variation in scale. In Fig. 18(b), we have shown the region allowed after the constraints from $g_\mu - 2$ and $\text{BR}(h_{\text{SM}} \rightarrow AA)$ are applied. We have seen from our earlier discussions that $g_\mu - 2$ favors large $\tan\beta$ while the upper limit on $\text{BR}(h_{\text{SM}} \rightarrow AA)$ favors low $\tan\beta$. λ_2 is inversely proportional to $\tan\beta$ in the alignment region. Therefore higher values of λ_2 are disfavored by the observed $g_\mu - 2$ data, while the lower λ_2 gets constrained from the $\text{BR}(h_{\text{SM}} \rightarrow AA)$.

In Fig. 18(c), we demonstrate regions with different levels of high-scale validity in the parameter space spanned by λ_1 and λ_3 . Their high-scale behavior appears to be strongly correlated with each other and the allowed range in the $\lambda_1 - \lambda_3$ plane shows elliptic contours. Figure 18(d) shows the allowed region after the imposition of $g_\mu - 2$ and $\text{BR}(h_{\text{SM}} \rightarrow AA)$ constraints. We can see that these two constraints do not affect these couplings directly, but only

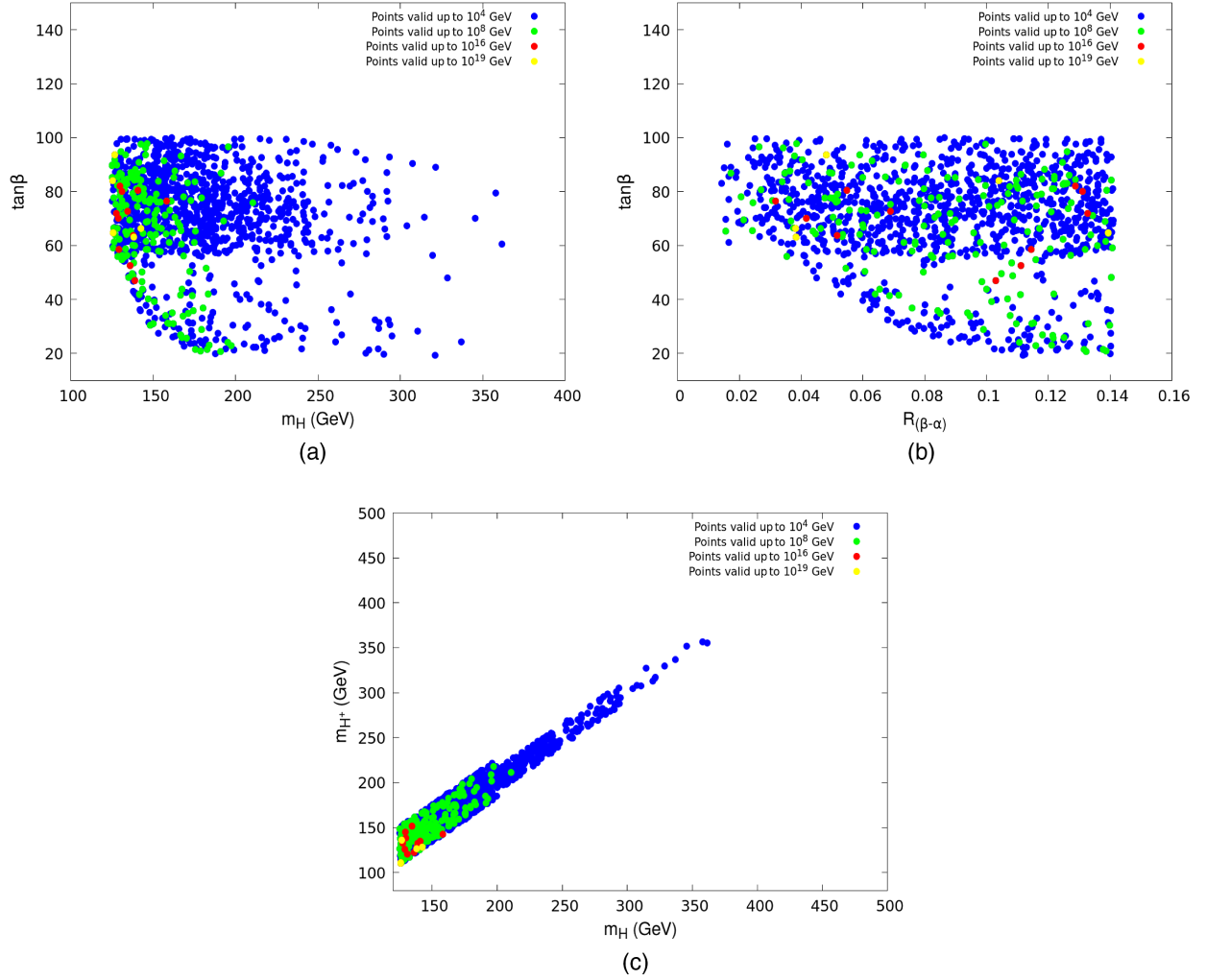


FIG. 17. (a) $m_H - \tan\beta$, (b) $R_{(\beta-\alpha)} - \tan\beta$, and (c) $m_H - m_{H^\pm}$ plane, valid up to different energy scales after applying theoretical constraints $+(g_\mu - 2)$ at $3\sigma + \text{BR}(h_{\text{SM}} \rightarrow AA)$ bounds for case 1.

reduces the density of points uniformly, depending on the other quartic couplings.

In Fig. 18(e), we plot the high-scale validity in the $\lambda_4 - \lambda_5$ plane. We have seen in our earlier discussion that the mass degeneracy between m_H and m_{H^\pm} implies $\lambda_4 \approx -\lambda_5$. As the perturbative unitarity condition favors this mass degeneracy, this correlation between λ_4 and λ_5 is also favored for high-scale validity. The $g_\mu - 2$ and $\text{BR}(h_{\text{SM}} \rightarrow AA)$ constraints result in only uniform reduction of allowed points, the nature of the allowed region remaining unaltered [see Fig. 18(f)].

It is clear from the discussion in the plane of quartic couplings that, the requirement of validity of the theory up to higher scales, pushes the quartic couplings to smaller values.

B. Case 2

In Fig. 19, we show the high-scale validity in $m_A - \tan\beta$ plane in the right-sign region of scenario 1. Here the nature

of high-scale validity is same as case 1 and for the same reason. The black line in the Fig. 19(a) denotes the lower limit coming from the $g_\mu - 2$ data. We have shown only the region $m_A > \frac{m_h}{2}$ here, because from the upper limit on $\text{BR}(h_{\text{SM}} \rightarrow AA)$, this is the only allowed region in this case, as discussed in Sec. V.

In Figs. 20(a)–20(c) we show the high-scale validity in the $(m_H - \tan\beta)$, $(R_{(\beta-\alpha)} - \tan\beta)$, and $(m_H - m_{H^\pm})$ planes, respectively, after imposing the $g_\mu - 2$ constraints and the upper limit from $\text{BR}(h_{\text{SM}} \rightarrow AA)$. Here too, we observe similar behavior as case 1 and the same discussion follows. We note here that, $\tan\beta \lesssim 50$ is completely disfavored in this case unlike case 1. The reason behind this is in case 2, we do not have a region with $m_A \lesssim \frac{m_h}{2}$ that satisfies the upper limit on $\text{BR}(h_{\text{SM}} \rightarrow AA)$ and $m_A > \frac{m_h}{2}$ region gets severely constrained by the lower limit from $g_\mu - 2$ when $\tan\beta \lesssim 50$.

We report next on the high-scale validity in the RS region of scenario 1 in the parameter space spanned by the quartic

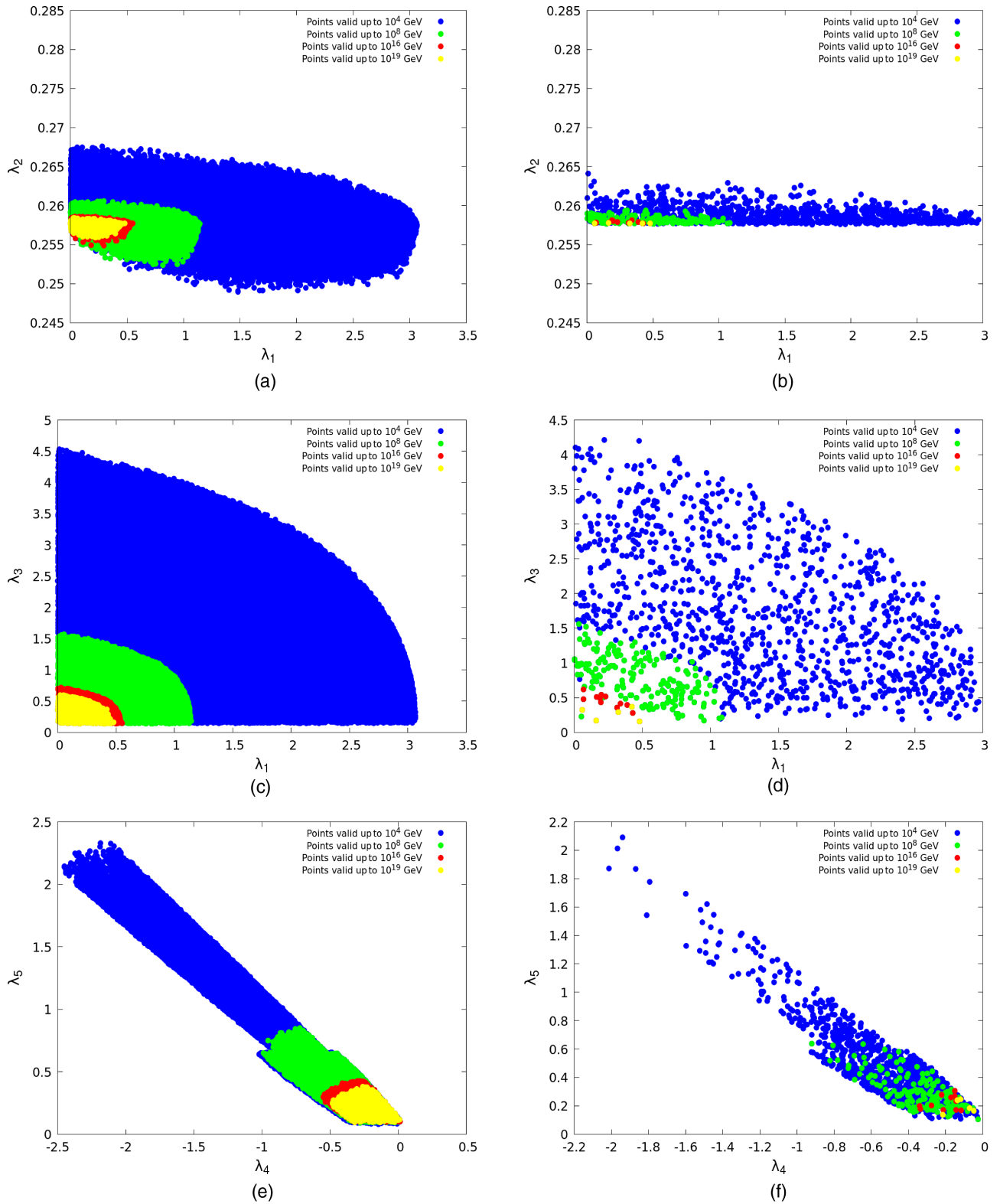


FIG. 18. Quartic couplings valid up to different energy scales after applying (a), (c), and (e) theoretical constraints and (b), (d), and (f) theoretical constraints + $(g_\mu - 2)$ at $3\sigma + \text{BR}(h_{\text{SM}} \rightarrow AA)$ bounds for case 1.

couplings. In Figs. 21(a)–21(f), we see similar features as in case 1. However, in this case, large values of λ_3 become disfavored even at the electroweak scale as can be seen

from Figs. 21(c) and 21(d), since in the RS case a stronger upper bound is imposed on the m_{H^\pm} and m_H , compared to WS case, in the pseudoscalar mass range of our interest.

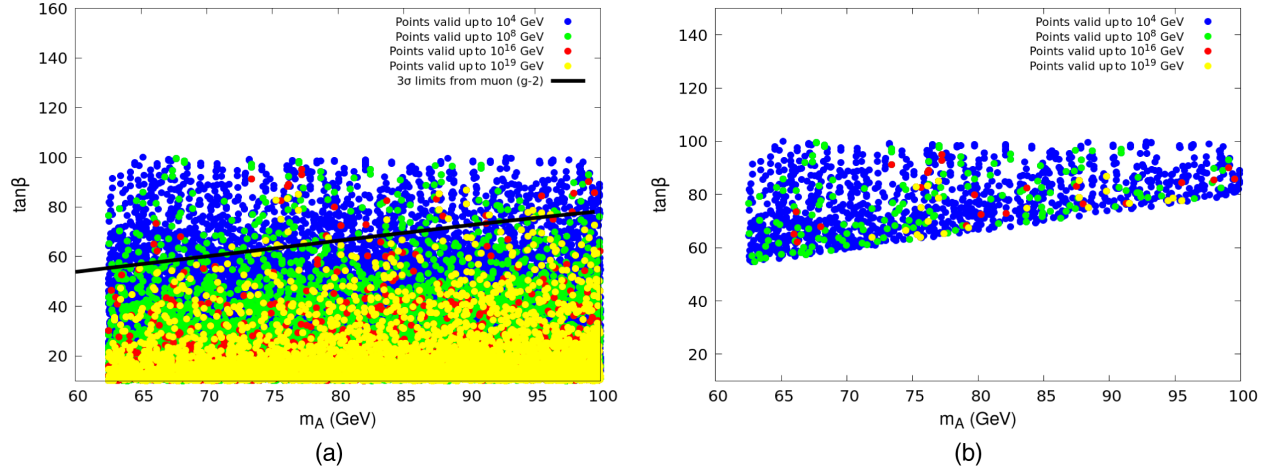


FIG. 19. $m_A - \tan\beta$ plane, valid up to different energy scales after applying (a) theoretical constraints (b) theoretical constraints + $(g_\mu - 2)$ at $3\sigma + \text{BR}(h_{\text{SM}} \rightarrow AA)$ bounds for case 2.

In Figs. 21(e) and 21(f), we see, in this case, that the lower masses of m_H and m_{H^\pm} restrict the upper limits on λ_4 and λ_5 to lower values compared to the WS case.

C. Case 3

We now proceed to scenario 2 (i.e., $m_H = 125$ GeV), in the WS region. In scenario 2, the charged scalar and the

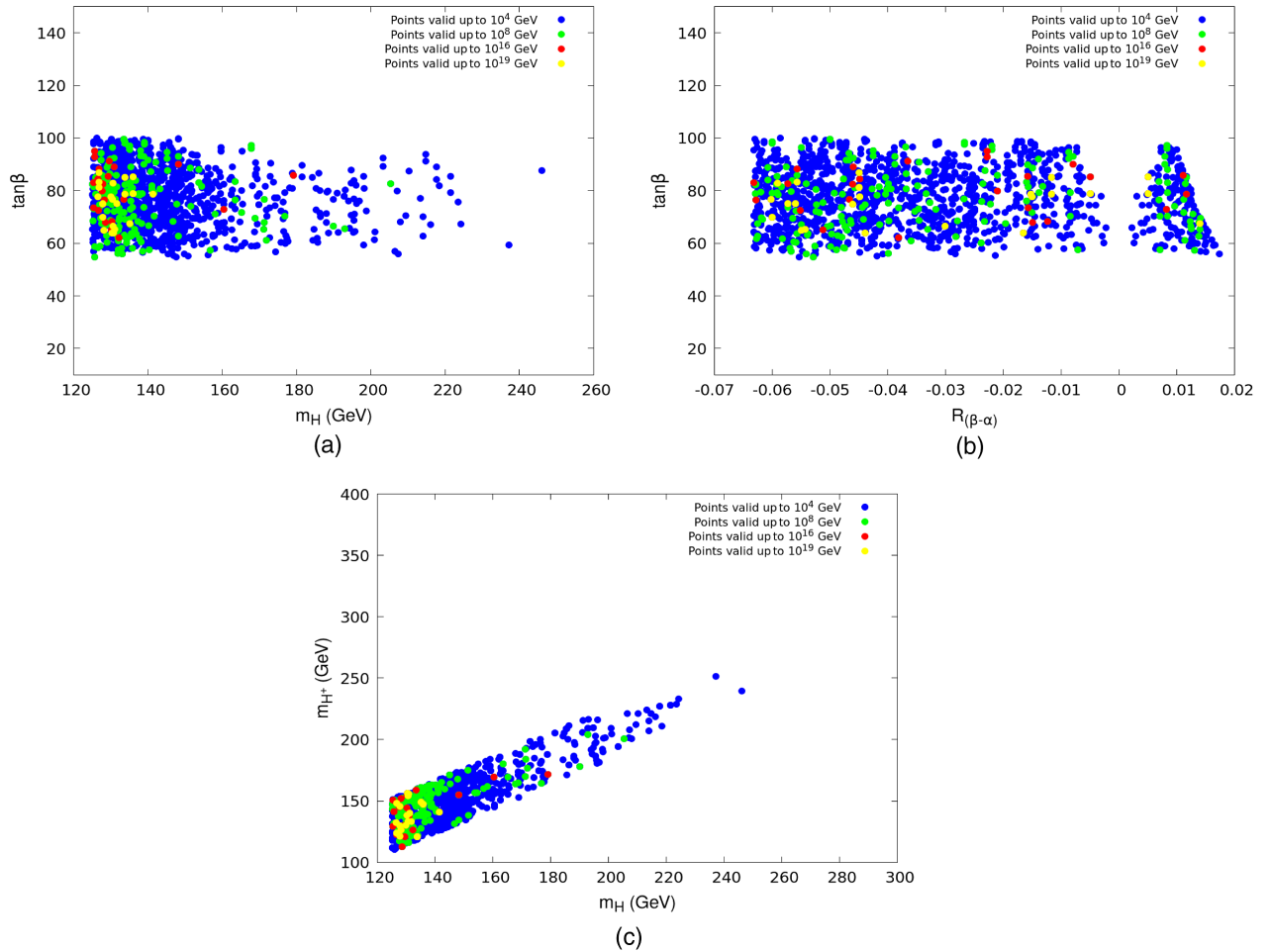


FIG. 20. (a) $m_H - \tan\beta$, (b) $R_{(\beta-\alpha)} - \tan\beta$, and (c) $m_h - m_{H^\pm}$ plane, valid up to different energy scales after applying theoretical constraints + $(g_\mu - 2)$ at $3\sigma + \text{BR}(h_{\text{SM}} \rightarrow AA)$ bounds for case 2.

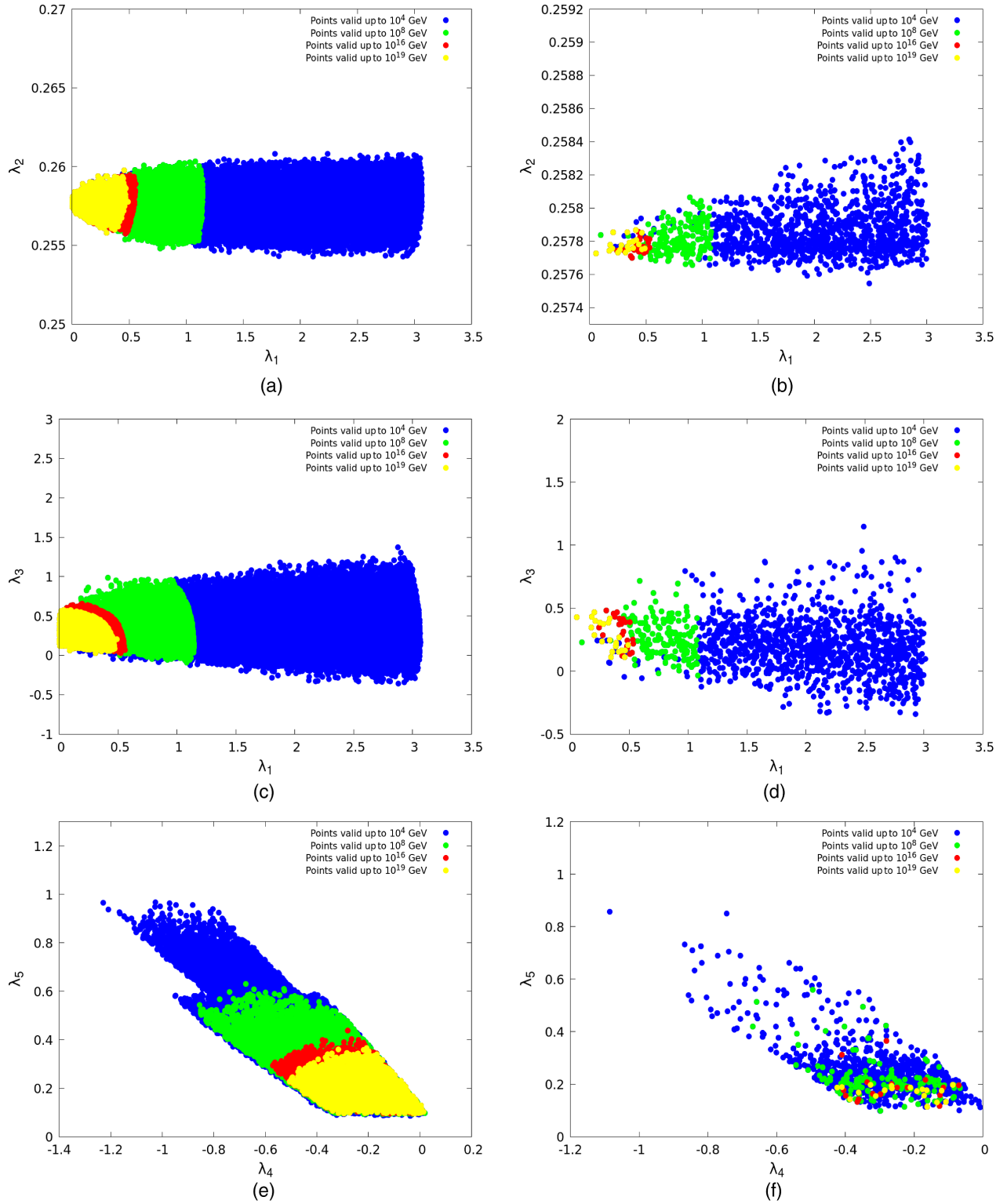


FIG. 21. Quartic couplings valid up to different energy scales after applying (a), (c), and (e) theoretical constraints and (b), (d), and (f) theoretical constraints + $(g_\mu - 2)$ at $3\sigma + \text{BR}(h_{\text{SM}} \rightarrow AA)$ bounds for case 2.

nonstandard CP -even scalar masses are kept at a lower range compared to scenario 1. In Fig. 22, we show the high-scale validity in the $m_A - \tan\beta$ plane. Like the previous cases, here too, the tension between the high-scale validity and the

observed $g_\mu - 2$ continues. We have not shown the region $m_A \lesssim \frac{m_H}{2}$ in Fig. 22, because in scenario 2, WS region, this region does not satisfy $\text{BR}(h_{\text{SM}} \rightarrow AA)$ upper limit. On the other hand, $m_A > \frac{m_H}{2}$ trivially satisfies this bound.

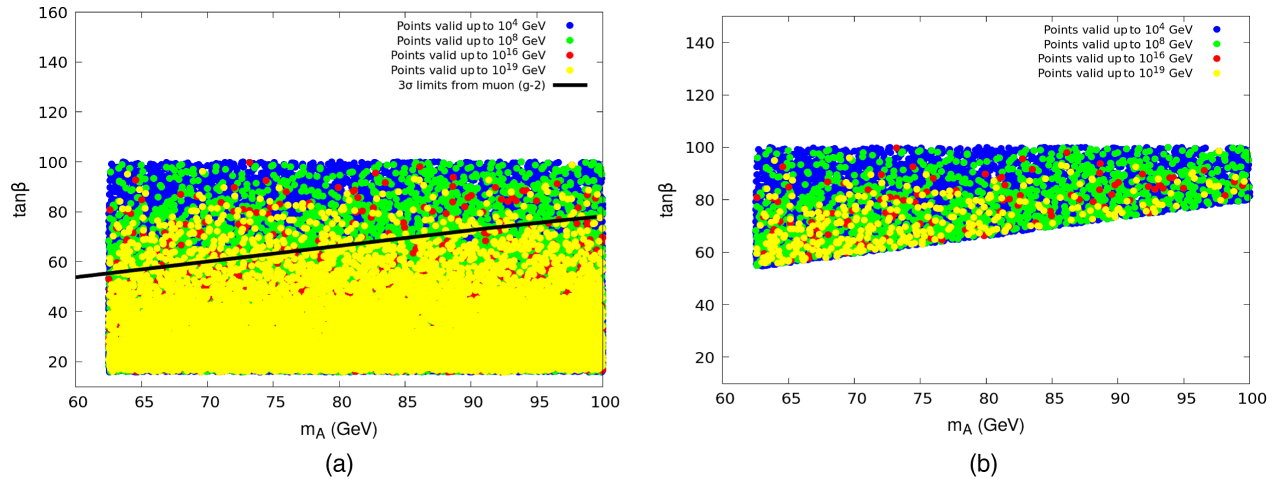


FIG. 22. $m_A - \tan\beta$ plane, valid up to different energy scales after applying (a) theoretical constraints (b) theoretical constraints + $(g_\mu - 2)$ at $3\sigma + \text{BR}(h_{\text{SM}} \rightarrow AA)$ bounds for case 3.

In Figs. 23(a)–23(c), we show the parameter space allowed by all the aforementioned constraints in the $(m_h - \tan\beta)$, $(\sin(\beta - \alpha) - \tan\beta)$, and $(m_h - m_{H^\pm})$ plane, respectively.

As a low mass range for the nonstandard CP -even scalar (h) is considered in this case, the entire mass range is valid up to very high scales. However, the $g_\mu - 2$ data disfavors the region

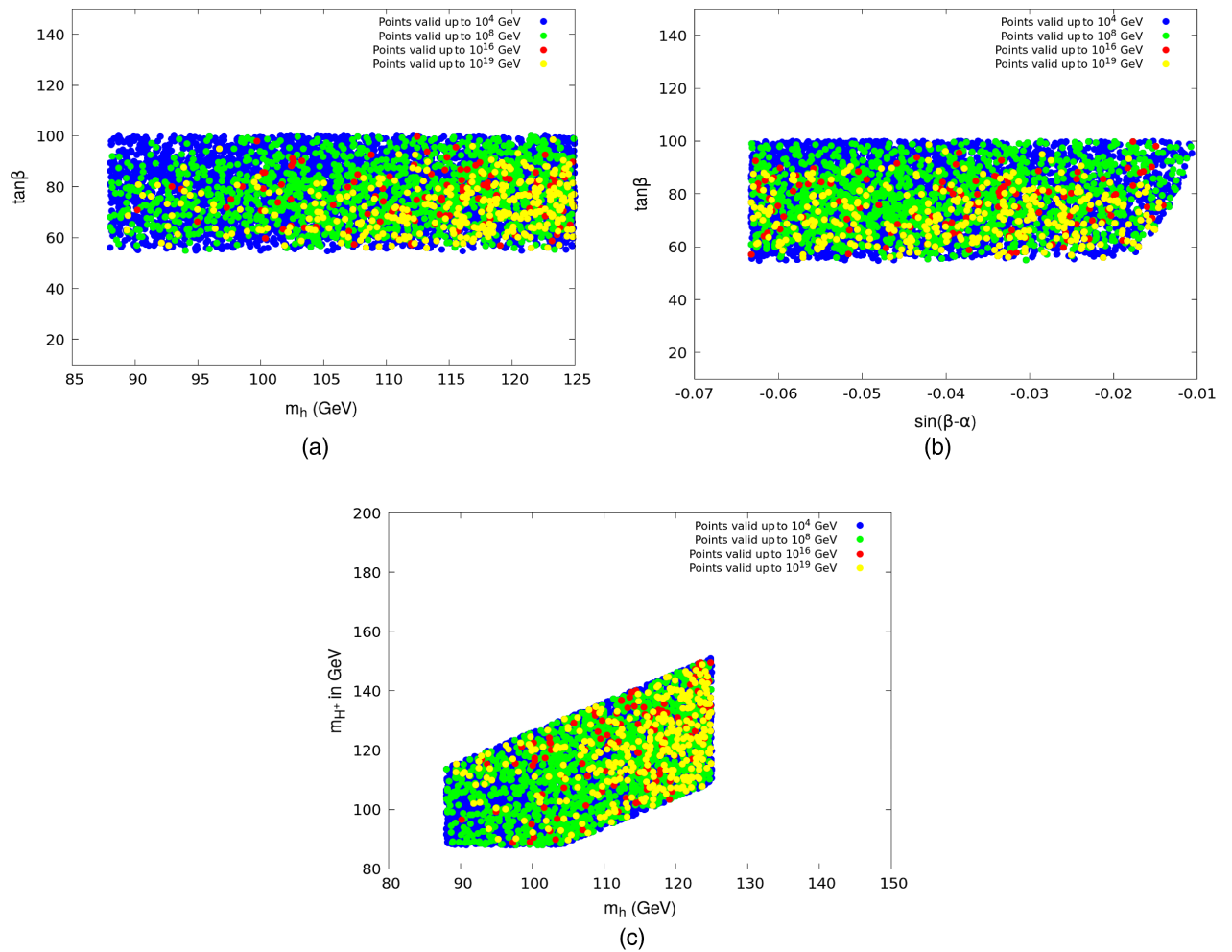


FIG. 23. (a) $m_h - \tan\beta$, (b) $\sin(\beta - \alpha) - \tan\beta$, and (c) $m_h - m_{H^\pm}$ plane, valid up to different energy scales after applying theoretical constraints + $(g_\mu - 2)$ at $3\sigma + \text{BR}(h_{\text{SM}} \rightarrow AA)$ bounds for case 3.

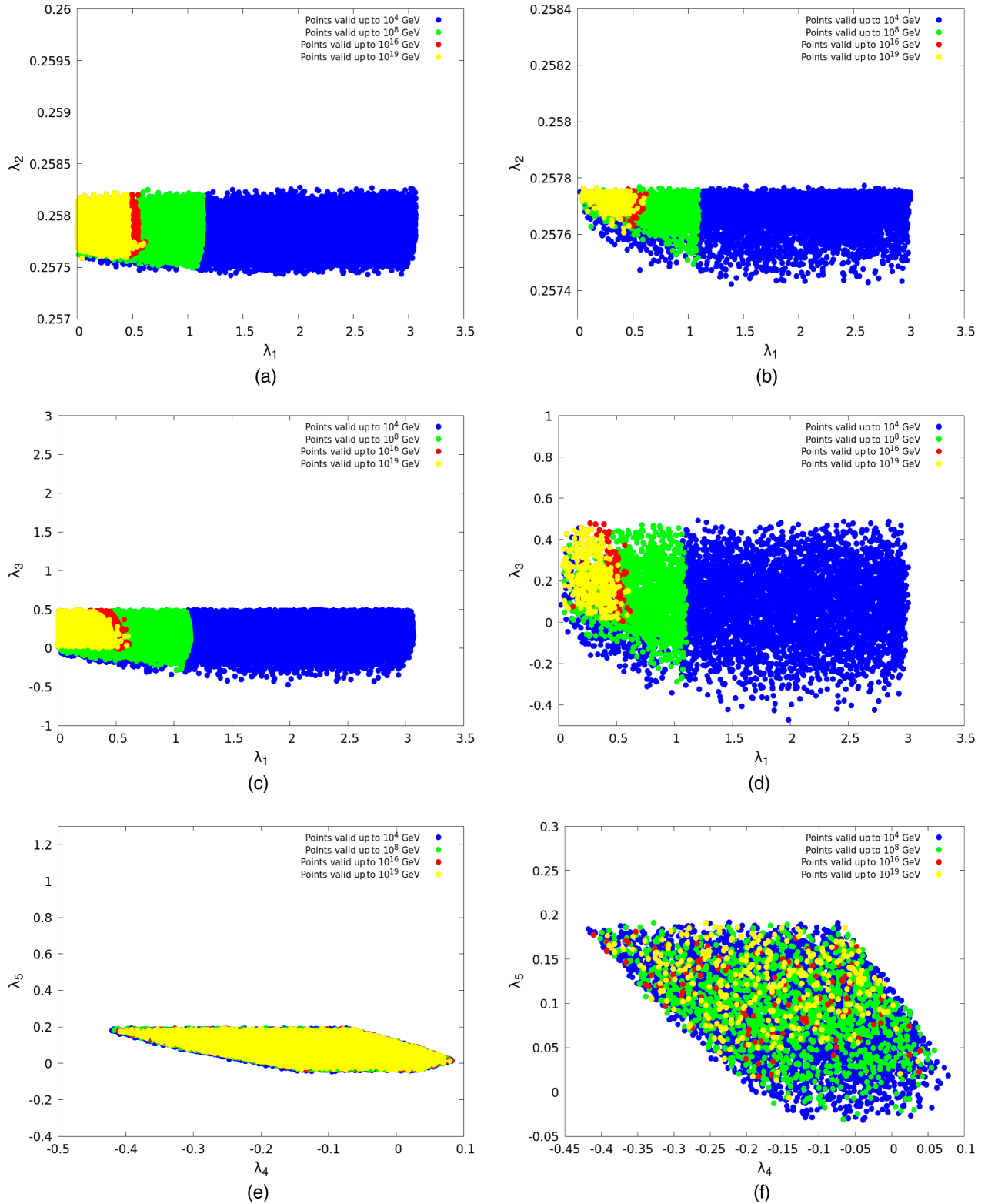


FIG. 24. Quartic couplings valid up to different energy scales after applying (a), (c), and (e) theoretical constraints and (b), (d), and (f) theoretical constraints $+(g_\mu - 2)$ at $3\sigma + \text{BR}(h_{\text{SM}} \rightarrow AA)$ bounds for case 3.

below $\tan \beta \lesssim 50$ for $m_A > \frac{m_h}{2}$ whereas $m_A \lesssim \frac{m_h}{2}$ is disfavored from the upper limit on $\text{BR}(h_{\text{SM}} \rightarrow AA)$, therefore we see no point in the range $\tan \beta \lesssim 50$ in Figs. 23(a) and 23(b).

The behavior of the quartic couplings in the context of high-scale validity is similar to the previous cases considered, as we can see from Figs. 24(a)–24(f). The apparently

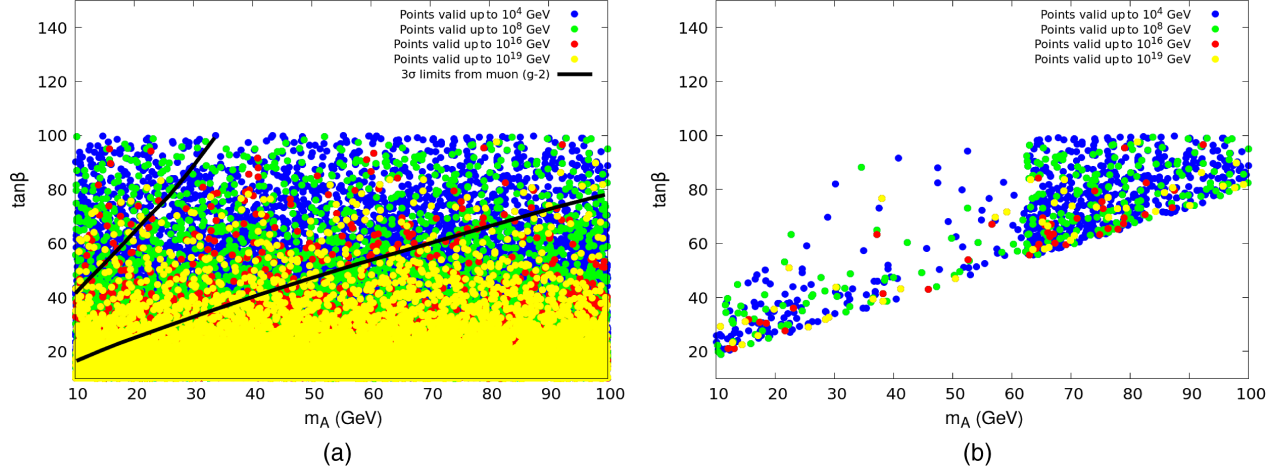


FIG. 25. $m_A - \tan\beta$ plane, valid up to different energy scales after applying (a) theoretical constraints and (b) theoretical constraints + $(g_\mu - 2)$ at $3\sigma + \text{BR}(h_{\text{SM}} \rightarrow AA)$ bounds for case 4.

stronger upper limit on λ_3 in Figs. 24(c) and 24(d) follows from the fact that the CP -even nonstandard scalar mass (m_h) is much lower in scenario 2, compared to scenario 1,

irrespective of WS and RS. In Figs. 24(e) and 24(f), we see a different behavior compared to scenario 1. The correlation between λ_4 and λ_5 here is not very clear. The reason

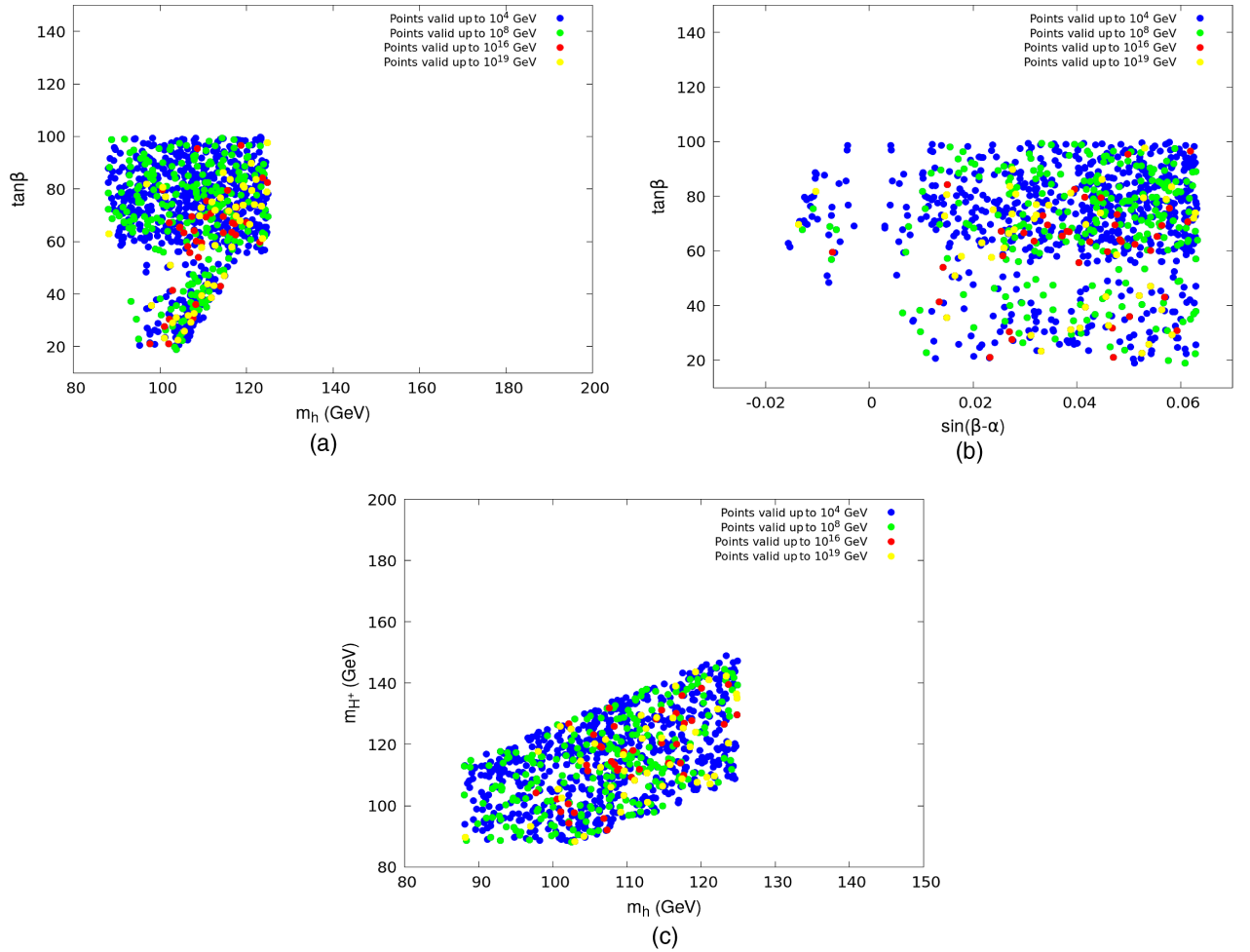


FIG. 26. (a) $m_h - \tan\beta$, (b) $\sin(\beta - \alpha) - \tan\beta$, and (c) $m_h - m_{H^\pm}$ plane, valid up to different energy scales after applying theoretical constraints + $(g_\mu - 2)$ at $3\sigma + \text{BR}(h_{\text{SM}} \rightarrow AA)$ bounds for case 4.

again is the following: In scenario 2, we are confined within a small range for m_h and therefore the degeneracy, which is responsible for the correlation between λ_4 and λ_5 , is not

very apparent in this case. As the nonstandard scalar masses are already small, almost the entire region considered is allowed up to a very high scale (10^{19} GeV).

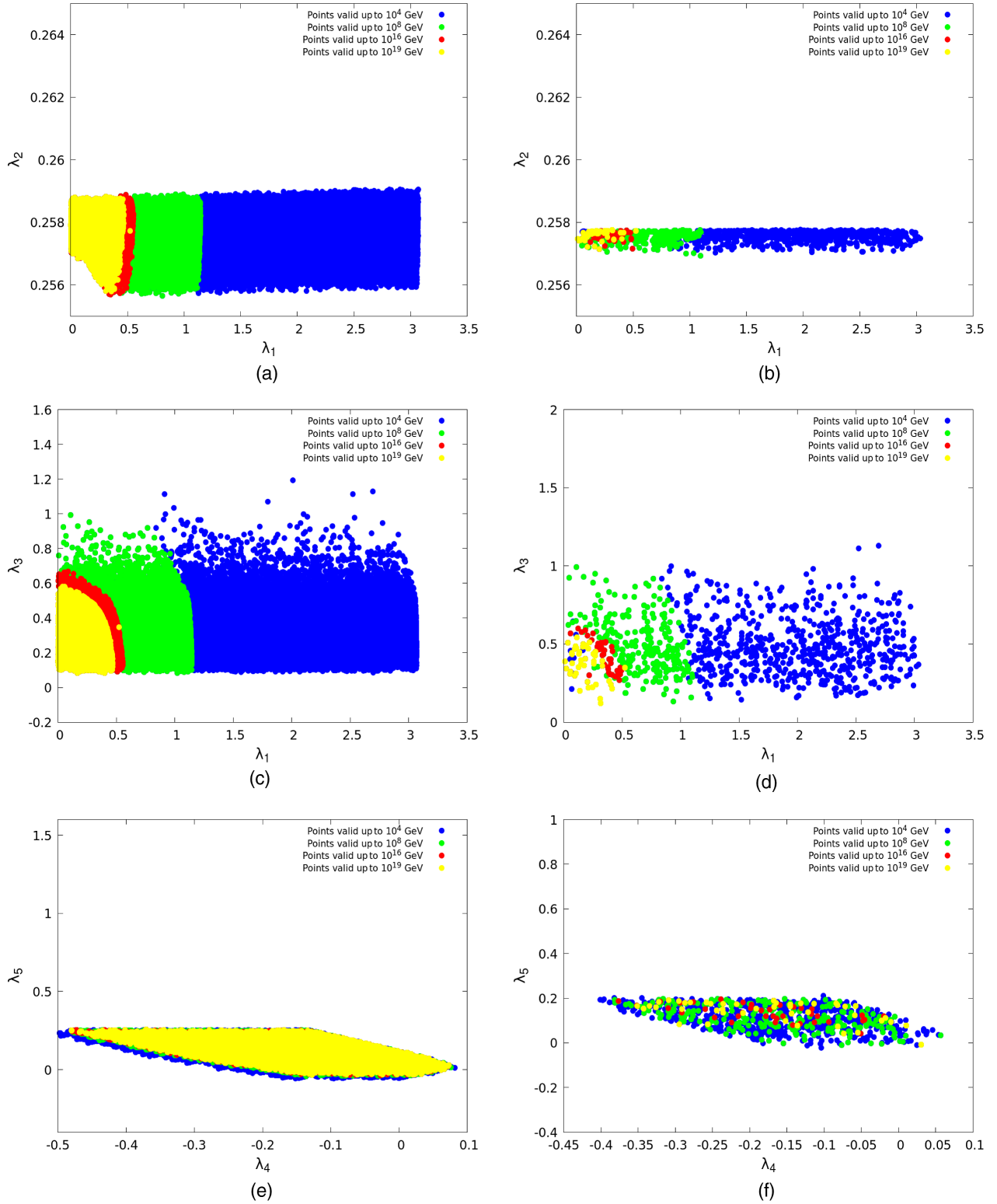


FIG. 27. Quartic couplings valid up to different energy scales after applying (a), (c), and (e) theoretical constraints and (b), (d), and (f) theoretical constraints + $(g_\mu - 2)$ at $3\sigma + \text{BR}(h_{\text{SM}} \rightarrow AA)$ bounds for case 4.

D. Case 4

Now we will focus on the RS region of scenario 2, i.e., $m_H = 125$ GeV. Here too, the charged Higgs and the nonstandard CP -even scalar masses are kept on the lower side. In Fig. 25, similar behavior as the previous cases is observed. One may note, similar to case 1, here we get a small region in the range $m_A \lesssim \frac{m_H}{2}$, mostly in the low $\tan\beta$, which satisfies the constraint from $\text{BR}(h_{\text{SM}} \rightarrow AA)$.

In Figs. 26(a)–26(c), we show the allowed parameter space in the plane spanned by $(m_h - \tan\beta)$, $(\sin(\beta - \alpha) - \tan\beta)$, and $(m_h - m_{H^\pm})$ plane, respectively. Due to low mass range of the nonstandard scalars, the entire mass range considered is valid up to very high scales just like in case 3. The strip below $\tan\beta \lesssim 50$ in Figs. 26(a) and 26(b) corresponds to the points with $m_A \lesssim \frac{m_H}{2}$, which satisfies the limit from $\text{BR}(h_{\text{SM}} \rightarrow AA)$, as we have argued in case 1.

We show next the region of parameter space in the plane of the quartic couplings, in Figs. 27(a)–27(f). The qualitative natures of the allowed regions are very similar to case 3, precisely because of low nonstandard scalar masses in both cases.

The most salient points of the discussion in the current section can be summarized as follows:

- (i) Irrespective of the specific case at hand, the smaller the quartic couplings are at the electroweak scale, the higher is the scale of validity of a theory.
- (ii) The requirement of small quartic couplings naturally implies moderate $\tan\beta$ and/or nonstandard scalar masses on the lower side.
- (iii) The observed $g_\mu - 2$ data favor large $\tan\beta$, creating a tension with high-scale validity.
- (iv) λ_1 (also λ_3 , although in a correlated manner with λ_1) and λ_5 (λ_4 shows a strong correlation with it), mainly control the high-scale behavior and remain practically unaffected by the constraints such as $g_\mu - 2$ or the $\text{BR}(h_{\text{SM}} \rightarrow AA)$.
- (v) λ_2 , on the other hand, does not play a significant role in the high-scale validity, but remains heavily constrained from $g_\mu - 2$ and $\text{BR}(h_{\text{SM}} \rightarrow AA)$.
- (vi) High-scale validity in general demands degeneracy between the nonstandard scalar masses as well as their closeness to the 125-GeV Higgs mass.
- (vii) In case 2, i.e., when the lighter CP -even scalar is SM-like in the right-sign region, the requirement of perturbative unitarity at the electroweak scale already favors lower nonstandard scalar masses and consequently lower quartic couplings, facilitating high-scale validity.
- (viii) In scenario 2 (both cases 3 and 4), i.e., the non-decoupling scenario, the nonstandard scalar masses are on the lower side, as compared to scenario 1. Therefore, here too, a major portion of the parameter space remains valid up to the Planck scale.
- (ix) Case 1 is least favored among the four cases considered, when high-scale validity is demanded.

Taking a cue from the above observations, we can now identify the regions in the type-X parameter space, which can be valid up to the GUT or Planck scale. Thus we may say that scenarios corresponding to such regions can become part of a grand unified framework without requiring any additional fields. On the other hand, the regions that encounter cutoffs at lower energies require the intervention of additional physics if has to be part of a grander design in its UV completion. Moreover, certain regions in the low energy parameter space are subject to unitarity limits at the scale of a few TeV itself. Therefore, one may expect to see collider signals for further new physics if observations ever indicate that one has type-X 2HDM corresponding to such parameter values.

VII. CONCLUSION

We have explored the high-scale validity of type-X 2HDM, particularly in regions of the parameter space answering to a low-mass neutral CP -odd spinless particle. Such a pseudoscalar is not only consistent with all experimental limits so far but can also help in explaining the observed discrepancy in $g_\mu - 2$. The high-scale validity of the regions of the parameter space of this model, where the above features of special interest are noticed, has been studied here.

We have identified the regions in the parameter space, which are helpful in explaining $(g_\mu - 2)$ including the most recent results. Other theoretical and experimental constraints, starting from low-scale perturbative unitarity, vacuum stability etc., and all the way to the most recent LHC limits, have been used to filter out the surviving parameter regions. The two-loop running of various couplings in such regions up to high scales has been studied thereafter, thus identifying regions where perturbative unitarity and vacuum stability are satisfied up to various high scales, ranging from 10^4 GeV to the Planck scale. Different benchmark points have been used, including both situations where the 125 GeV state is either the lighter or the heavier neutral CP -even scalar. Scenarios with both right- and wrong-sign Yukawa couplings have also been scanned across the parameter space.

For regions in the parameter space having cutoff scales on the lower side, the aspiration for perturbative unification of the three SM gauge couplings is found to necessitate UV completion of type-X 2HDM below the GUT scale. For regions with perturbative validity inching up to the Planck scale, on the other hand, the requirements for gauge coupling unification turn out to be similar to what they are for the standard model electroweak symmetry breaking sector. All this bears ample testimony to the type-X 2HDM being a candidate theory that explains the observed value of $g_\mu - 2$, keeping open a rich set of UV completion possibilities.

ACKNOWLEDGMENTS

We thank Amitava Raychaudhuri for useful discussions. This work was partially supported by funding available from the Department of Atomic Energy, Government of India, for the Regional Centre for Accelerator-based

Particle Physics (RECAPP), Harish-Chandra Research Institute. B. M. would like to thank RECAPP, HRI, where a significant part of the work was done. A. D. and J. L. would like to thank Indian Institute of Science Education and Research, Kolkata, where part of the work was done.

-
- [1] G. W. Bennett *et al.* (Muon $g - 2$ Collaboration), Final report of the muon E821 anomalous magnetic moment measurement at BNL, *Phys. Rev. D* **73**, 072003 (2006).
- [2] B. Abi *et al.* (Muon $g - 2$ Collaboration), Measurement of the Positive Muon Anomalous Magnetic Moment to 0.46 ppm, *Phys. Rev. Lett.* **126**, 141801 (2021).
- [3] T. Albahri *et al.* (Muon $g - 2$ Collaboration), Measurement of the anomalous precession frequency of the muon in the Fermilab Muon $g - 2$ Experiment, *Phys. Rev. D* **103**, 072002 (2021).
- [4] J. Cao, P. Wan, L. Wu, and J. M. Yang, Lepton-specific two-Higgs doublet model: Experimental constraints and implication on Higgs phenomenology, *Phys. Rev. D* **80**, 071701 (2009).
- [5] A. Arhrib, C.-W. Chiang, D. K. Ghosh, and R. Santos, Two Higgs doublet model in light of the standard model $H \rightarrow \tau^+ \tau^-$ search at the LHC, *Phys. Rev. D* **85**, 115003 (2012).
- [6] L. Wang and X.-F. Han, A light pseudoscalar of 2HDM confronted with muon $g - 2$ and experimental constraints, *J. High Energy Phys.* **05** (2015) 039.
- [7] A. Crivellin, J. Heeck, and P. Stoffer, A Perturbed Lepton-Specific Two-Higgs-Doublet Model Facing Experimental Hints for Physics Beyond the Standard Model, *Phys. Rev. Lett.* **116**, 081801 (2016).
- [8] T. Abe, R. Sato, and K. Yagyu, Lepton-specific two Higgs doublet model as a solution of muon $g - 2$ anomaly, *J. High Energy Phys.* **07** (2015) 064.
- [9] X. Liu, L. Bian, X.-Q. Li, and J. Shu, Type-III two Higgs doublet model plus a pseudoscalar confronted with $h \rightarrow \mu\tau$, muon $g - 2$ and dark matter, *Nucl. Phys.* **B909**, 507 (2016).
- [10] E. J. Chun, S. Dwivedi, T. Mondal, and B. Mukhopadhyaya, Reconstructing a light pseudoscalar in the Type-X Two Higgs Doublet Model, *Phys. Lett. B* **774**, 20 (2017).
- [11] E. J. Chun, S. Dwivedi, T. Mondal, B. Mukhopadhyaya, and S. K. Rai, Reconstructing heavy Higgs boson masses in a type X two-Higgs-doublet model with a light pseudoscalar particle, *Phys. Rev. D* **98**, 075008 (2018).
- [12] N. Chakrabarty, C.-W. Chiang, T. Ohata, and K. Tsumura, Charged scalars confronting neutrino mass and muon $g - 2$ anomaly, *J. High Energy Phys.* **12** (2018) 104.
- [13] L. Wang, J. M. Yang, M. Zhang, and Y. Zhang, Revisiting lepton-specific 2HDM in light of muon $g - 2$ anomaly, *Phys. Lett. B* **788**, 519 (2019).
- [14] S. Iguro, Y. Omura, and M. Takeuchi, Testing the 2HDM explanation of the muon $g - 2$ anomaly at the LHC, *J. High Energy Phys.* **11** (2019) 130.
- [15] E. J. Chun, J. Kim, and T. Mondal, Electron EDM and Muon anomalous magnetic moment in Two-Higgs-Doublet Models, *J. High Energy Phys.* **12** (2019) 068.
- [16] P. Bandyopadhyay, E. J. Chun, and R. Mandal, Phenomenology of Higgs bosons in inverse seesaw model with Type-X two Higgs doublet at the LHC, *J. High Energy Phys.* **08** (2019) 169.
- [17] M. Frank and I. Saha, Muon anomalous magnetic moment in two Higgs doublet models with vector-like leptons, *Phys. Rev. D* **102**, 115034 (2020).
- [18] J. E. Chun and T. Mondal, Explaining $g - 2$ anomalies in two Higgs doublet model with vector-like leptons, *J. High Energy Phys.* **11** (2020) 077.
- [19] A. Jueid, J. Kim, S. Lee, and J. Song, Type-X two Higgs doublet model in light of the muon $g - 2$: confronting Higgs and collider data, *Phys. Rev. D* **104**, 095008 (2021).
- [20] M. Endo, K. Hamaguchi, S. Iwamoto, and T. Kitahara, Supersymmetric interpretation of the muon $g - 2$ anomaly, *J. High Energy Phys.* **07** (2021) 075.
- [21] O. M. Boyarkin, G. G. Boyarkina, and V. V. Makhnach, $(g - 2)_\mu$ anomaly within the left-right symmetric model, *Phys. Rev. D* **77**, 033004 (2008).
- [22] R. Dermisek, K. Hermanek, and N. McGinnis, Muon $g - 2$ in two-Higgs-doublet models with vectorlike leptons, *Phys. Rev. D* **104**, 055033 (2021).
- [23] G. Mohlabeng, Revisiting the dark photon explanation of the muon anomalous magnetic moment, *Phys. Rev. D* **99**, 115001 (2019).
- [24] C.-H. Chen, C.-W. Chiang, and T. Nomura, Muon $g - 2$ in a two-Higgs-doublet model with a type-II seesaw mechanism, *Phys. Rev. D* **104**, 055011 (2021).
- [25] J. a. P. Pinheiro, C. A. de S. Pires, F. S. Queiroz, and Y. S. Villamizar, Confronting the inverse seesaw mechanism with the recent muon $g - 2$ result, *Phys. Lett. B* **823**, 136764 (2021).
- [26] G. C. Branco, P. M. Ferreira, L. Lavoura, M. N. Rebelo, M. Sher, and J. P. Silva, Theory and phenomenology of two-Higgs-doublet models, *Phys. Rep.* **516**, 1 (2012).
- [27] X.-F. Han and H.-X. Wang, Revisiting wrong sign Yukawa coupling of type II two-Higgs-doublet model in light of recent LHC data, *Chin. Phys. C* **44**, 013002 (2020).
- [28] A. M. Sirunyan *et al.* (CMS Collaboration), Combined measurements of Higgs boson couplings in proton-proton collisions at $\sqrt{s} = 13\text{TeV}$, *Eur. Phys. J. C* **79**, 421 (2019).
- [29] G. Aad *et al.* (ATLAS Collaboration), Combined measurements of Higgs boson production and decay using up to 80fb^{-1} of proton-proton collision data at $\sqrt{s} = 13\text{TeV}$

- collected with the ATLAS experiment, *Phys. Rev. D* **101**, 012002 (2020).
- [30] T. Blum, A. Denig, I. Logashenko, E. de Rafael, B. L. Roberts, T. Teubner *et al.*, The muon $(g - 2)$ theory value: Present and future, [arXiv:1311.2198](https://arxiv.org/abs/1311.2198).
- [31] H. Iinuma (J-PARC muon $g - 2$ /EDM Collaboration), New approach to the muon $g - 2$ and EDM experiment at J-PARC, *J. Phys. Conf. Ser.* **295**, 012032 (2011).
- [32] M. Davier, A. Hoecker, B. Malaescu, and Z. Zhang, Reevaluation of the hadronic contributions to the muon $g - 2$ and to $\alpha(M_Z^2)$, *Eur. Phys. J. C* **71** (2011). 1515.
- [33] K. Hagiwara, R. Liao, A. D. Martin, D. Nomura, and T. Teubner, $(g - 2)_\mu$ and $\alpha(M_Z^2)$ re-evaluated using new precise data, *J. Phys. G* **38**, 085003 (2011).
- [34] M. Davier, A. Hoecker, B. Malaescu, and Z. Zhang, Reevaluation of the hadronic vacuum polarisation contributions to the Standard Model predictions of the muon $g - 2$ and $\alpha(m_Z^2)$ using newest hadronic cross-section data, *Eur. Phys. J. C* **77**, 827 (2017).
- [35] M. Davier, A. Hoecker, B. Malaescu, and Z. Zhang, A new evaluation of the hadronic vacuum polarisation contributions to the muon anomalous magnetic moment and to $\alpha(m_Z^2)$, *Eur. Phys. J. C* **80**, 241 (2020).
- [36] A. Keshavarzi, D. Nomura, and T. Teubner, Muon $g - 2$ and $\alpha(M_Z^2)$: A new data-based analysis, *Phys. Rev. D* **97**, 114025 (2018).
- [37] G. Colangelo, M. Hoferichter, and P. Stoffer, Two-pion contribution to hadronic vacuum polarization, *J. High Energy Phys.* **02** (2019) 006.
- [38] M. Hoferichter, B.-L. Hoid, and B. Kubis, Three-pion contribution to hadronic vacuum polarization, *J. High Energy Phys.* **08** (2019) 137.
- [39] A. Keshavarzi, D. Nomura, and T. Teubner, $g - 2$ of charged leptons, $\alpha(M_Z^2)$, and the hyperfine splitting of muonium, *Phys. Rev. D* **101**, 014029 (2020).
- [40] A. Kurz, T. Liu, P. Marquard, and M. Steinhauser, Hadronic contribution to the muon anomalous magnetic moment to next-to-next-to-leading order, *Phys. Lett. B* **734**, 144 (2014).
- [41] K. Melnikov and A. Vainshtein, Hadronic light-by-light scattering contribution to the muon anomalous magnetic moment revisited, *Phys. Rev. D* **70**, 113006 (2004).
- [42] P. Masjuan and P. Sanchez-Puertas, Pseudoscalar-pole contribution to the $(g_\mu - 2)$: A rational approach, *Phys. Rev. D* **95**, 054026 (2017).
- [43] G. Colangelo, M. Hoferichter, M. Procura, and P. Stoffer, Dispersion relation for hadronic light-by-light scattering: Two-pion contributions, *J. High Energy Phys.* **04** (2017) 161.
- [44] M. Hoferichter, B.-L. Hoid, B. Kubis, S. Leupold, and S. P. Schneider, Dispersion relation for hadronic light-by-light scattering: Pion pole, *J. High Energy Phys.* **10** (2018) 141.
- [45] A. Gérardin, H. B. Meyer, and A. Nyffeler, Lattice calculation of the pion transition form factor with $N_f = 2 + 1$ Wilson quarks, *Phys. Rev. D* **100**, 034520 (2019).
- [46] J. Bijnens, N. Hermansson-Truedsson, and A. Rodríguez-Sánchez, Short-distance constraints for the HLbL contribution to the muon anomalous magnetic moment, *Phys. Lett. B* **798**, 134994 (2019).
- [47] G. Colangelo, F. Hagelstein, M. Hoferichter, L. Laub, and P. Stoffer, Longitudinal short-distance constraints for the hadronic light-by-light contribution to $(g - 2)_\mu$ with large- N_c Regge models, *J. High Energy Phys.* **03** (2020) 101.
- [48] G. Colangelo, M. Hoferichter, A. Nyffeler, M. Passera, and P. Stoffer, Remarks on higher-order hadronic corrections to the muon $g - 2$, *Phys. Lett. B* **735**, 90 (2014).
- [49] T. Blum, N. Christ, M. Hayakawa, T. Izubuchi, L. Jin, C. Jung, and C. Lehner, Hadronic Light-by-Light Scattering Contribution to the Muon Anomalous Magnetic Moment from Lattice QCD, *Phys. Rev. Lett.* **124**, 132002 (2020).
- [50] T. Aoyama, M. Hayakawa, T. Kinoshita, and M. Nio, Complete Tenth-Order QED Contribution to the Muon $g - 2$, *Phys. Rev. Lett.* **109**, 111808 (2012).
- [51] A. Czarnecki, W. J. Marciano, and A. Vainshtein, Refinements in electroweak contributions to the muon anomalous magnetic moment, *Phys. Rev. D* **67**, 073006 (2003).
- [52] T. Aoyama, T. Kinoshita, and M. Nio, Theory of the anomalous magnetic moment of the electron, *Atoms* **7**, 28 (2019).
- [53] C. Gnendiger, D. Stöckinger, and H. Stöckinger-Kim, The electroweak contributions to $(g - 2)_\mu$ after the Higgs boson mass measurement, *Phys. Rev. D* **88**, 053005 (2013).
- [54] P. A. Zyla *et al.* (Particle Data Group Collaboration), Review of Particle Physics, *Prog. Theor. Exp. Phys.* **2020**, 083C01 (2020).
- [55] T. Aoyama *et al.*, The anomalous magnetic moment of the muon in the Standard Model, *Phys. Rep.* **887**, 1 (2020).
- [56] S. Borsanyi, Z. Fodor, C. Hoelbling, T. Kawanai, S. Krieg, L. Lellouch, R. Malak, K. Miura, K. K. Szabo, C. Torrero, and B. C. Toth (Budapest-Marseille-Wuppertal Collaboration), Hadronic Vacuum Polarization Contribution to the Anomalous Magnetic Moments of Leptons from First Principles, *Phys. Rev. Lett.* **121**, 022002 (2018).
- [57] P. Roig and P. Sanchez-Puertas, Axial-vector exchange contribution to the hadronic light-by-light piece of the muon anomalous magnetic moment, *Phys. Rev. D* **101**, 074019 (2020).
- [58] N. Asmussen, E.-H. Chao, A. Gérardin, J. R. Green, R. J. Hudspith, H. B. Meyer *et al.*, Developments in the position-space approach to the HLbL contribution to the muon $g - 2$ on the lattice, *Proc. Sci.*, LATTICE2019 (2019) 195 [[arXiv:1911.05573](https://arxiv.org/abs/1911.05573)].
- [59] F. S. Queiroz and W. Shepherd, New physics contributions to the muon anomalous magnetic moment: A numerical code, *Phys. Rev. D* **89**, 095024 (2014).
- [60] V. Ilisie, New Barr-Zee contributions to $(g - 2)_\mu$ in two-Higgs-doublet models, *J. High Energy Phys.* **04** (2015) 077.
- [61] A. Broggio, E. J. Chun, M. Passera, K. M. Patel, and S. K. Vempati, Limiting two-Higgs-doublet models, *J. High Energy Phys.* **11** (2014) 058.
- [62] A. Cherchiglia, D. Stöckinger, and H. Stöckinger-Kim, Muon $g - 2$ in the 2HDM: Maximum results and detailed phenomenology, *Phys. Rev. D* **98**, 035001 (2018).
- [63] P. Athron, C. Balázs, D. H. Jacob, W. Kotlarski, D. Stöckinger, and H. Stöckinger-Kim, New physics explanations of a_μ in light of the FNAL muon $g - 2$ measurement, *J. High Energy Phys.* **09** (2021) 080.
- [64] M. Baak (Gfitter Collaboration), Review of electroweak fits of the SM and beyond, after the Higgs discovery—with Gfitter, *Proc. Sci.*, EPS-HEP2013 (2013) 203.

- [65] J. Haller, A. Hoecker, R. Kogler, K. Mönig, T. Peiffer, and J. Stelzer, Update of the global electroweak fit and constraints on two-Higgs-doublet models, *Eur. Phys. J. C* **78**, 675 (2018).
- [66] I. Maksymyk, C. P. Burgess, and D. London, Beyond S, T and U, *Phys. Rev. D* **50**, 529 (1994).
- [67] A. Kundu and P. Roy, A general treatment of oblique parameters, *Int. J. Mod. Phys. A* **12**, 1511 (1997).
- [68] G. Funk, D. O’Neil, and R. M. Winters, What the oblique parameters S, T, and U and their extensions reveal about the 2HDM: A numerical analysis, *Int. J. Mod. Phys. A* **27**, 1250021 (2012).
- [69] D. Eriksson, J. Rathsman, and O. Stal, 2HDMC: Two-Higgs-doublet model calculator physics and manual, *Comput. Phys. Commun.* **181**, 189 (2010).
- [70] H.-J. He, N. Polonsky, and S.-f. Su, Extra families, Higgs spectrum and oblique corrections, *Phys. Rev. D* **64**, 053004 (2001).
- [71] W. Grimus, L. Lavoura, O. M. Ogreid, and P. Osland, A precision constraint on multi-Higgs-doublet models, *J. Phys. G* **35**, 075001 (2008).
- [72] G. Bhattacharyya and D. Das, Scalar sector of two-Higgs-doublet models: A minireview, *Pramana* **87**, 40 (2016).
- [73] Y. Amhis *et al.* (Heavy Flavor Averaging Group (HFAG) Collaboration), Averages of b -hadron, c -hadron, and τ -lepton properties as of summer 2014, [arXiv:1412.7515](https://arxiv.org/abs/1412.7515).
- [74] A. Crivellin, A. Kokulu, and C. Greub, Flavor-phenomenology of two-Higgs-doublet models with generic Yukawa structure, *Phys. Rev. D* **87**, 094031 (2013).
- [75] A. Arbey, F. Mahmoudi, O. Stal, and T. Stefaniak, Status of the charged Higgs boson in two higgs doublet models, *Eur. Phys. J. C* **78**, 182 (2018).
- [76] M. Hussain, M. Usman, M. A. Paracha, and M. J. Aslam, Constraints on two Higgs doublet model parameters in the light of rare B -decays, *Phys. Rev. D* **95**, 075009 (2017).
- [77] D. A. Dicus and V. S. Mathur, Upper bounds on the values of masses in unified gauge theories, *Phys. Rev. D* **7**, 3111 (1973).
- [78] B. W. Lee, C. Quigg, and H. B. Thacker, The Strength of Weak Interactions at Very High-Energies and the Higgs Boson Mass, *Phys. Rev. Lett.* **38**, 883 (1977).
- [79] N. G. Deshpande and E. Ma, Pattern of symmetry breaking with two Higgs doublets, *Phys. Rev. D* **18**, 2574 (1978).
- [80] S. Nie and M. Sher, Vacuum stability bounds in the two Higgs doublet model, *Phys. Lett. B* **449**, 89 (1999).
- [81] J. F. Gunion and H. E. Haber, The CP conserving two Higgs doublet model: The approach to the decoupling limit, *Phys. Rev. D* **67**, 075019 (2003).
- [82] P. M. Ferreira, J. F. Gunion, H. E. Haber, and R. Santos, Probing wrong-sign Yukawa couplings at the LHC and a future linear collider, *Phys. Rev. D* **89**, 115003 (2014).
- [83] E. J. Chun, Z. Kang, M. Takeuchi, and Y.-L. S. Tsai, LHC τ -rich tests of lepton-specific 2HDM for $(g-2)_{\mu}$, *J. High Energy Phys.* **11** (2015) 099.
- [84] G. Abbiendi *et al.* (ALEPH, DELPHI, L3, OPAL, LEP Collaboration), Search for charged Higgs bosons: combined results using LEP data, *Eur. Phys. J. C* **73**, 2463 (2013).
- [85] J. Abdallah *et al.* (DELPHI Collaboration), Searches for neutral higgs bosons in extended models, *Eur. Phys. J. C* **38**, 1 (2004).
- [86] S. Kanemura, K. Tsumura, and H. Yokoya, Multi-tau-lepton signatures at the LHC in the two Higgs doublet model, *Phys. Rev. D* **85**, 095001 (2012).
- [87] S. Kanemura, K. Tsumura, K. Yagyu, and H. Yokoya, Fingerprinting nonminimal Higgs sectors, *Phys. Rev. D* **90**, 075001 (2014).
- [88] A. M. Sirunyan *et al.* (CMS Collaboration), Search for an exotic decay of the Higgs boson to a pair of light pseudoscalars in the final state of two muons and two τ leptons in proton-proton collisions at $\sqrt{s} = 13$ TeV, *J. High Energy Phys.* **11** (2018) 018.
- [89] J. Bernon, J. F. Gunion, Y. Jiang, and S. Kraml, Light Higgs bosons in Two-Higgs-Doublet Models, *Phys. Rev. D* **91**, 075019 (2015).
- [90] V. Khachatryan *et al.* (CMS Collaboration), Search for a low-mass pseudoscalar Higgs boson produced in association with a $b\bar{b}$ pair in pp collisions at $\sqrt{s} = 8$ TeV, *Phys. Lett. B* **758**, 296 (2016).
- [91] A. M. Sirunyan *et al.* (CMS Collaboration), Search for a low-mass $\tau^+\tau^-$ resonance in association with a bottom quark in proton-proton collisions at $\sqrt{s} = 13$ TeV, *J. High Energy Phys.* **05** (2019) 210.
- [92] V. Khachatryan *et al.* (CMS Collaboration), Search for neutral MSSM Higgs bosons decaying into a pair of bottom quarks, *J. High Energy Phys.* **11** (2015) 071.
- [93] CMS Collaboration, Search for a narrow heavy decaying to bottom quark pairs in the 13 TeV data sample, Report No. CMS-PAS-HIG-16-025.
- [94] V. Khachatryan *et al.* (CMS Collaboration), Search for neutral resonances decaying into a Z boson and a pair of b jets or τ leptons, *Phys. Lett. B* **759**, 369 (2016).
- [95] CMS Collaboration, Search for H to Z(II) + A(bb) with 2015 data, Report No. CMS-PAS-HIG-16-010.
- [96] A. M. Sirunyan *et al.* (CMS Collaboration), Search for resonant pair production of Higgs bosons decaying to bottom quark-antiquark pairs in proton-proton collisions at 13 TeV, *J. High Energy Phys.* **08** (2018) 152.
- [97] A. M. Sirunyan *et al.* (CMS Collaboration), Search for Higgs boson pair production in the $\gamma\gamma b\bar{b}$ final state in pp collisions at $\sqrt{s} = 13$ TeV, *Phys. Lett. B* **788**, 7 (2019).
- [98] M. Aaboud *et al.* (ATLAS Collaboration), Search for pair production of Higgs bosons in the $b\bar{b}b\bar{b}$ final state using proton-proton collisions at $\sqrt{s} = 13$ TeV with the ATLAS detector, *J. High Energy Phys.* **01** (2019) 030.
- [99] ATLAS Collaboration, Search for a high-mass Higgs boson decaying to a pair of W bosons in pp collisions at $\sqrt{s} = 13$ TeV with the ATLAS detector, Report No. ATLAS-CONF-2016-074.
- [100] ATLAS Collaboration, Search for high-mass resonances decaying into a Z boson pair in the $\ell\ell\nu\nu$ final state in pp collisions at $\sqrt{s} = 13$ TeV with the ATLAS detector, Report No. ATLAS-CONF-2016-012.
- [101] G. Aad *et al.* (ATLAS Collaboration), Search for resonances decaying into photon pairs in 139 fb^{-1} of pp collisions at $\sqrt{s} = 13$ TeV with the ATLAS detector, *Phys. Lett. B* **822**, 136651 (2021).
- [102] G. Aad *et al.* (ATLAS Collaboration), Search for charged Higgs bosons decaying via $H^\pm \rightarrow \tau^\pm\nu$ in fully hadronic final states using pp collision data at

- $\sqrt{s} = 8$ TeV with the ATLAS detector, *J. High Energy Phys.* **03** (2015) 088.
- [103] V. Khachatryan *et al.* (CMS Collaboration), Search for a charged Higgs boson in pp collisions at $\sqrt{s} = 8$ TeV, *J. High Energy Phys.* **11** (2015) 018.
- [104] G. Aad *et al.* (ATLAS Collaboration), Search for a light charged Higgs boson in the decay channel $H^+ \rightarrow c\bar{s}$ in $t\bar{t}$ events using pp collisions at $\sqrt{s} = 7$ TeV with the ATLAS detector, *Eur. Phys. J. C* **73**, 2465 (2013).
- [105] V. Khachatryan *et al.* (CMS Collaboration), Search for a light charged Higgs boson decaying to $c\bar{s}$ in pp collisions at $\sqrt{s} = 8$ TeV, *J. High Energy Phys.* **12** (2015) 178.
- [106] M. Aaboud *et al.* (ATLAS Collaboration), Search for charged Higgs bosons produced in association with a top quark and decaying via $H^\pm \rightarrow \tau\nu$ using pp collision data recorded at $\sqrt{s} = 13$ TeV by the ATLAS detector, *Phys. Lett. B* **759**, 555 (2016).
- [107] ATLAS Collaboration, Search for charged Higgs bosons in the τ + jets final state using 14.7 fb^{-1} of pp collision data recorded at of pp collision data recorded at $\sqrt{s} = 13$ TeV with the ATLAS experiment, Report No. ATLAS-CONF-2016-088.
- [108] CMS Collaboration, Search for charged Higgs bosons with the $H^\pm \rightarrow \tau^\pm\nu_\tau$ decay channel in the fully hadronic final state at $\sqrt{s} = 13$ TeV, Report No. CMS-PAS-HIG-16-031.
- [109] ATLAS Collaboration, Search for charged Higgs bosons in the $H^\pm \rightarrow tb$ decay channel in pp collisions at $\sqrt{s} = 13$ TeV using the ATLAS detector, Report No. ATLAS-CONF-2016-089.
- [110] M. Aaboud *et al.* (ATLAS Collaboration), Search for additional heavy neutral Higgs and gauge bosons in the ditau final state produced in 36 fb^{-1} of pp collisions at $\sqrt{s} = 13$ TeV with the ATLAS detector, *J. High Energy Phys.* **01** (2018) 055.
- [111] A. M. Sirunyan *et al.* (CMS Collaboration), Search for additional neutral MSSM Higgs bosons in the $\tau\tau$ final state in proton-proton collisions at $\sqrt{s} = 13$ TeV, *J. High Energy Phys.* **09** (2018) 007.
- [112] G. Aad *et al.* (ATLAS Collaboration), Search for Heavy Higgs Bosons Decaying into Two Tau Leptons with the ATLAS Detector Using pp Collisions at $\sqrt{s} = 13$ TeV, *Phys. Rev. Lett.* **125**, 051801 (2020).
- [113] A. M. Sirunyan *et al.* (CMS Collaboration), Search for charged Higgs bosons in the $H^\pm \rightarrow \tau^\pm\nu_\tau$ decay channel in proton-proton collisions at $\sqrt{s} = 13$ TeV, *J. High Energy Phys.* **07** (2019) 142.
- [114] D. Chowdhury and O. Eberhardt, Global fits of the two-loop renormalized Two-Higgs-Doublet model with soft Z_2 breaking, *J. High Energy Phys.* **11** (2015) 052.